Computer Methods in Applied Mechanics and Engineering 432 (2024) 117346

Contents lists available at ScienceDirect

Comput. Methods Appl. Mech. Engrg.

journal homepage: www.elsevier.com/locate/cma

A variational-based non-smooth contact dynamics approach for the seismic analysis of historical masonry structures

Nicola A. Nodargi *, Paolo Bisegna

Department of Civil Engineering and Computer Science, University of Rome Tor Vergata, via del Politecnico 1, Rome, 00133, Italy

ARTICLE INFO

Keywords:
Masonry
Rigid blocks
Dynamic analysis
Rocking behavior
Second-order cone programming
Seismic vulnerability

ABSTRACT

A variational formulation of the non-smooth contact dynamics method is proposed to address the dynamic response of historical masonry structures modeled as systems of 3D rigid blocks and subjected to ground excitation. Upon assuming a unilateral-frictional contact law between the blocks, the equations of motions are formulated in a time-discrete impulse theorem format in the unknown block velocities and contact impulses. The variational structure of the problem to be solved at each time step is proven. On that basis, the numerical method requires at each time step to perform a collision detection that identifies antagonist contact points based on the given structural configuration, to solve a second-order conic programming problem that outputs block velocities and contact impulses, and to update the structural configuration for the solution to advance in time. As a merit of the formulation, large-scale problems can be robustly and efficiently addressed thanks to the convex setting of the time-step optimization problem. Numerical results are presented to test the computational performances of the proposed approach. Benchmark problems provide numerical evidence that the formulation is consistent with event-driven solutions based on the classical Housner impact model. The dynamic response, failure domains, and fragility functions of real-size masonry structures are then explored under ground impulse or earthquake excitation. The obtained results prove the reliability of the present computational method for the dynamic analysis and seismic assessment of historical masonry constructions of engineering interest.

1. Introduction

Historical masonry constructions represent a valuable part of the architectural heritage, whose structural safety in seismic regions could be endangered by earthquakes. Prompted by the need for their preservation, a reliable assessment of the seismic vulnerability of those constructions is required, based on predicting their dynamic response when subjected to ground acceleration.

Historical masonry constructions can be modeled as systems of rigid blocks in dry contact with each other (if mortar was initially present, for safety, it is assumed as completely deteriorated) [1–3]. In its essence, their dynamic behavior is thus exemplified by the rocking motion of a single 2D rigid block under ground excitation, as first studied in a seminal work by Housner [4]. The rocking motion consists of a sequence of smooth motion phases, in which the block rotates about one of its bottom corners, alternated by impacts against the supporting plane, implying a switch of the basis pivotal point. Following Housner's derivation of the equation of motion of the block at smooth time instants and of the kinetic energy dissipation due to instantaneous and perfectly inelastic impacts, the single-block rocking problem has been extensively explored (e.g., see [5–21]). Generalizations have been later on considered to describe the dynamic behavior of multi-block 2D masonry structures, either simplified as single-degree-of-freedom

* Corresponding author.
E-mail address: nodargi@ing.uniroma2.it (N.A. Nodargi).

https://doi.org/10.1016/j.cma.2024.117346
Received 25 June 2024; Received in revised form 18 August 2024; Accepted 27 August 2024
Available online 3 September 2024

systems (e.g., see [22–29]) or treated as multi-degree-of-freedom systems (e.g., see [30–35]). In addition, the spatial rocking motion of a single 3D rigid block has been investigated (e.g., see [36–41]).

Due to the occurrence of impacts, i.e., of events producing velocity discontinuities, the rocking motion of block masonry structures represents a non-smooth dynamic problem. A rigorous mathematical formulation is thus obtained by assuming that the velocities are functions of bounded variation and by setting the equations of motion as a measure differential inclusion [42]. In the contributions mentioned above, an event-driven scheme is adopted for its numerical solution (e.g., see [43,44]). That requires (i) integrating the equations of smooth motion until some interpenetration between the blocks is detected, marking the end of the smooth motion phase; (ii) determining the precise instant of impact; and (iii) solving an impact problem at the instant of impact in preparation to the next smooth motion phase. While tasks (i) and (iii) are theoretically sound and can be efficiently performed (for 2D systems, a variational formulation amounting to quadratic programming problems has been proposed [35]), task (ii) is generally more intricate. In fact, accurately locating an event in time makes it necessary to adopt some root-finding procedure, such as a sub-stepping scheme progressively adjusting the time step until a prescribed precision in the event detection is reached. In addition to the computational cost, numerical issues may arise when the rocking motion is characterized by a sequence of impacts not well-separated in time, as expected in complex multi-block masonry structures, or even possesses a finite accumulation point, as is the case of the so-called Zeno behavior [41,45].

In order to overcome those difficulties, a time-stepping scheme can be adopted instead of an event-driven one, i.e., a time-discretization method not explicitly considering the events occurring during the motion [43,44]. Specifically proposed by Moreau and Jean to investigate the dynamic behavior of collections of rigid bodies in contact with each other is the non-smooth contact dynamics (NSCD) method [42,46,47], whose fundamental idea is to address a discrete version of the time-integrated equations of motion. Resorting to such an impulse-theorem format has the crucial advantage that, alongside body velocities, contact impulses over a time step naturally emerge as the problem unknowns. Hence, by interpreting the contacts between the bodies in a time-averaged sense and by introducing suitable contact gaps in the contact relationships (to account for bodies that are close enough to be in potential contact at the end of the time step but are yet separated), the need for a precise identification of the event times is circumvented and the solution advances in time with a fixed time step.

Unilateral-frictional contacts have been considered within the NSCD method, as required in the dynamic analysis of block masonry structures, assuming (non-associative, i.e., non-dilatant) Coulomb friction law. The imposition of that friction law has been either achieved by tackling a nonlinear complementarity problem [47] or a linear complementarity problem based on a polyhedral approximation of the Coulomb cone [48] (for the numerical solution of those problems, fixed-point-iteration or first-order methods can be resorted to, e.g. see [43,49,50]). Within the polyhedral approximation strategy, a convergence result of the time-stepping method has also been derived to the solution of the underlying measure differential inclusion [51]. Several developments in the method have been proposed, e.g. dealing with the fulfillment of the frictional conditions both at velocity and position levels [52,53], the achievement of a higher-order time-stepping scheme [54–56], the consistency of the discrete time-step problem with the continuous one [57], or the numerical technique for the solution of the frictional contact conditions [58,59]. As an evolution of the original Jean implementation, the research software LMGC90 is currently available in the literature, which delivers an implementation of the NSCD method adopting a nonlinear block Gauss–Seidel algorithm for the solution of the time step problem [60]. Specifically, applications of the NSCD method to block masonry structures have been successfully considered using that software and its extensions, also addressing complex full-scale 3D constructions such as ancient masonry churches or towers (e.g., see [61–64]).

The solution of the complementarity problems required by the NSCD method to enforce the Coulomb friction law at contacts may be expensive due to their non-convexity. An interesting remedy has been offered in [65], based on the observation that if an associative (i.e., dilatant) Coulomb friction law is enforced instead of the non-associative one, the solution of the numerical method still converges, in the limit of vanishing time step, to the solution of the original non-associative problem. Roughly speaking, the dilatancy effect does not accumulate after the time step in which it arises, thus remaining bounded at a magnitude proportional to the time step [66]. By exploiting that idea, a variational format of the method has been proposed for 2D block masonry structures, exploiting the efficient computational solution of convex quadratic programming problems at each time step [67–71]. Concerning 3D block masonry structures, a regularization of the method has been proposed, resorting to a numerical compliance to avoid multiplicity of solutions in terms of contact impulses due to static indeterminacy [72–74].

While NSCD can be regarded as a distinct element method (DEM) [75], for it models a given structure as an assembly of distinct bodies, its peculiar feature is to be a non-smooth and implicit method. By converse, the label DEM is commonly referred to a broad class of smoothed and explicit methods, also applied to the dynamics of collections of rigid or deformable bodies in unilateral-frictional contact, that adopt a regularization technique to approximate the contact law by a nonlinear spring-damper element and resort to explicit time integration to address that nonlinear behavior [76]. Since steep penalty functions are usually needed to match the actual stiffness and dissipation properties of the contacts, short time-integration steps are generally required, and the solution is somewhat sensitive to the input material parameters, which are often uncertain and complex to measure by experiments. Nevertheless, the capability of DEM to predict the dynamic behavior of multi-block masonry columns, arches, and walls has been proven (e.g., see [77–81]). A detailed account of DEM application to masonry structures can be found in [82].

In the present work, a variational formulation of the non-smooth contact dynamics method is proposed for the dynamic analysis of historical masonry structures modeled as systems of 3D rigid blocks and subjected to ground excitation. Following the NSCD method, a discrete version of the time-integrated equations of motion is considered in the unknown block velocities and contact impulses. A unilateral-frictional contact law is assumed to govern the interactions between the blocks, which is enforced by constraining the relative velocity between pairs of antagonist contact points to belong to the kinematic Coulomb cone. Contact gaps are included

in the kinematic constraint to account for potential contacts at the beginning of each time step. By adopting an associative friction flow rule and exploiting the descending static-kinematic duality, it is shown that the equations of motion governing the dynamic evolution of the block system under prescribed external forces are obtained as the stationarity conditions of a saddle-point functional, from which purely kinematic and static functionals are obtained. Therefore, at the typical time step, the proposed method requires performing a collision detection algorithm to determine antagonist contact points based on the given configuration, solving a sparse second-order conic programming problem (SOCP) to compute block velocities and contact impulses, and updating the system configuration in preparation to the next time step. As the main novelty of the proposed method, the convex variational setting of the derived time-step problem allows for accomplishing enhanced robustness and efficiency compared to competing NSCD approaches in the literature and for strengthening the potentialities to solve large-scale three-dimensional problems. While comparing the performances of different types of solvers deserves further investigation, the optimization software Mosek® is adopted here to solve the required SOCP [83]. That implements a primal-dual interior-point method, which is designed to handle large-scale and sparse problems robustly and efficiently [84,85].

Numerical results are presented to investigate the computational performances of the proposed formulation. They include validation in three benchmark problems, dealing with the Housner block, a 3D rigid block, and a multi-block masonry arch, and three full-scale structural applications concerning a spandrel arch, a stone house, and a historical church. A thorough exploration is carried out on the dynamic response and failure domains of those systems to given ground impulse excitations. Moreover, in the stone-house problem, the structural response to earthquake excitation is studied by considering a family of ground motion records and providing relevant results in the form of structural fragility functions. Numerical applications finally prove the accuracy, robustness, and computational efficiency of the method, which enables the seismic analysis of real-size historical masonry constructions constituted by up to thousands of blocks.

The paper is organized as follows. In Section 2, the variational formulation of the NSCD problem for block masonry structure under ground excitation is presented. The adopted collision detection algorithm is discussed in Section 3. Numerical results are described in Section 4. Conclusions are outlined in Section 5. Details on the linearization of the time-discrete rotational equations of motion are given in Appendix.

2. Formulation

A system of B three-dimensional rigid blocks in unilateral-frictional contact is considered. The state of the system at time t is described within a prescribed reference frame by introducing the following variables:

$$\begin{aligned} &\mathbf{x} = \left(\mathbf{x}^1; \dots; \mathbf{x}^B\right), \quad \mathbf{R} = \operatorname{diag}\left(\mathbf{R}^1; \dots; \mathbf{R}^B\right), \\ &\mathbf{v} = \left(\mathbf{v}^1; \dots; \mathbf{v}^B\right), \quad \boldsymbol{\omega} = \left(\boldsymbol{\omega}^1; \dots; \boldsymbol{\omega}^B\right). \end{aligned} \tag{1}$$

For the typical block b, $\mathbf{x}^b$ and $\mathbf{R}^b$ respectively denote the coordinates of the block centroid G^b and the block rotation matrix, whereas $\mathbf{v}^b$ and $\boldsymbol{\omega}^b$ respectively denote the velocity of the block centroid and the block angular velocity. A semicolon indicates column-stacking, and diag stands for the operator forming a block-diagonal matrix with the indicated entries. For future use, the following positions are also introduced:

$$\boldsymbol{\Omega} = \operatorname{diag}\left(\boldsymbol{\Omega}^1; \dots; \boldsymbol{\Omega}^B\right), \quad \boldsymbol{\Omega}^b = \operatorname{skw} \boldsymbol{\omega}^b, \tag{2}$$

in which, for skw denoting the operator that forms the skew-symmetric matrix associated with the indicated vector, $\boldsymbol{\Omega}^b$ represents the angular velocity matrix of the block b.

2.1. Equations of motion

Upon resorting to a backward Euler method for discretization in time, the translational and rotational equations of motion for the block system at time $t = t_n + \Delta t$ are written in the following impulse-theorem format:

$$\begin{aligned} &\mathbf{M}\mathbf{v} - \mathbf{M}\mathbf{v}_n = \mathbf{f}\,\Delta t + \boldsymbol{\mathcal{F}}, \\ &\mathbf{J}\,\boldsymbol{\omega} - \mathbf{J}_n\,\boldsymbol{\omega}_n = \mathbf{c}\,\Delta t + \boldsymbol{C}, \end{aligned} \tag{3}$$

in the unknown velocities $\mathbf{v}$ and $\boldsymbol{\omega}$ at time t, for given velocities $\mathbf{v}_n$ and $\boldsymbol{\omega}_n$ at time t_n. In the left hand-side, the variation of linear and angular momenta of the block system within the time step Δt is stated. Here, the mass and inertia matrices of the block system, respectively denoted by $\mathbf{M}$ and $\mathbf{J}$, are constructed as:

$$\mathbf{M} = \operatorname{diag}\left(M^1\boldsymbol{I}; \dots; M^B\boldsymbol{I}\right), \quad \mathbf{J} = \mathbf{R}\,\tilde{\mathbf{J}}\,\mathbf{R}^T, \quad \tilde{\mathbf{J}} = \operatorname{diag}(\tilde{\mathbf{J}}^1; \dots; \tilde{\mathbf{J}}^B), \tag{4}$$

with M^b and $\tilde{\mathbf{J}}^b$ respectively as the mass and principal inertia matrices of the typical block b in the initial configuration, and $\boldsymbol{I}$ as the 3×3 identity matrix. Conversely, in the right hand-side, the resultant linear and angular impulses on the block system within the time step Δt are accounted for, with $\mathbf{f}$ and $\mathbf{c}$ as the external forces and couples, respectively, and $\boldsymbol{\mathcal{F}}$ and $\boldsymbol{C}$ as the contact linear and angular impulses, respectively. The equations of motion (3) are complemented by the following configuration update:

$$\mathbf{x} = \mathbf{x}_n + \mathbf{v}\,\Delta t, \quad \mathbf{R} = \exp\left(\boldsymbol{\Omega}\,\Delta t\right)\mathbf{R}_n. \tag{5}$$

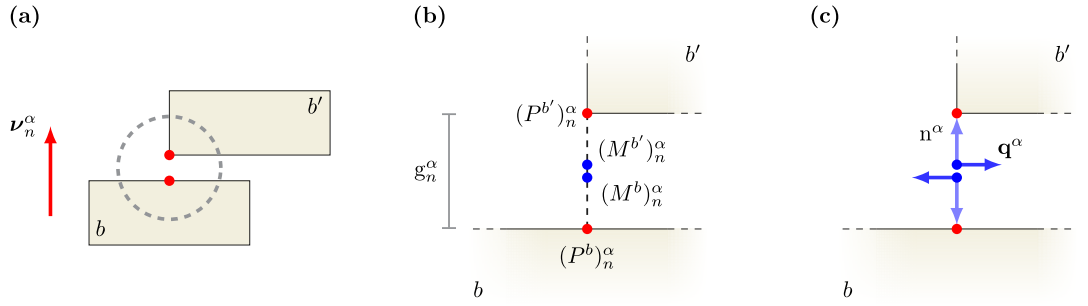

Fig. 1. Unilateral-frictional contacts: (a,b) typical potential contact between two blocks, with highlighted contact direction, antagonist contact points, and gap, and (c) parallel and orthogonal components of the contact impulse. Unilateral-frictional constraints are enforced at the mid-point between the antagonist contact points for self-equilibrated internal contact impulses to be obtained.

It is recalled that, while the mass matrix $\mathbf{M}$ is constant in time, the inertia matrix $\mathbf{J}$ is not, thus making the rotational equation of motion $(3)_2$ nonlinear. The following quasi-Newton scheme is adopted for its solution:

$$\mathbf{J}^*\boldsymbol{\omega}^* + \mathbf{H}^*\left(\boldsymbol{\omega} - \boldsymbol{\omega}^*\right) - \mathbf{J}_n\,\boldsymbol{\omega}_n = \mathbf{c}\,\Delta t + \boldsymbol{C}, \tag{6}$$

in which $\boldsymbol{\omega}^*$ denotes the previous iterate for the unknown angular velocity $\boldsymbol{\omega}$ and $\mathbf{H}^*$ denotes the positive semidefinite part of the Jacobian of the nonlinear map $\boldsymbol{\omega} \mapsto \mathbf{J}\boldsymbol{\omega}$ at the previous iterate (for its computation, see Appendix). Eq. (6) is recast as:

$$\mathbf{H}^*\boldsymbol{\omega} - \mathbf{H}^*\boldsymbol{\omega}_n = \mathbf{c}\,\Delta t + \boldsymbol{C} + \mathbf{h}^*, \quad \mathbf{h}^* = \mathbf{H}^*\left(\boldsymbol{\omega}^* - \boldsymbol{\omega}_n\right) - \left(\mathbf{J}^*\boldsymbol{\omega}^* - \mathbf{J}_n\,\boldsymbol{\omega}_n\right), \tag{7}$$

where $\mathbf{h}^*$ is interpreted as an unbalanced angular momentum. In light of such a scheme, at the typical iteration, the equilibrium equations $(3)_1$ and (7) need to be solved. They can be compactly written as:

$$\boldsymbol{H}^*\left(\boldsymbol{v} - \boldsymbol{v}_n\right) = \boldsymbol{b}\,\Delta t + \boldsymbol{\mathcal{I}} + \boldsymbol{h}^*, \tag{8}$$

in which generalized velocities, external forces, and contact impulses have been introduced by:

$$\boldsymbol{v} = (\mathbf{v};\,\boldsymbol{\omega}), \quad \boldsymbol{b} = (\mathbf{f};\,\mathbf{c}), \quad \boldsymbol{\mathcal{I}} = (\boldsymbol{\mathcal{F}};\,\boldsymbol{C}), \tag{9}$$

with the generalized velocities to be possibly accompanied by no subscript, a subscript n, or a superscript * to respectively denote values at time t, at time t_n, or values at the previous iterate. Moreover, the generalized Jacobian approximation and unbalanced momenta have been introduced by:

$$\boldsymbol{H}^* = \mathrm{diag}\left(\mathbf{M};\,\mathbf{H}^*\right), \quad \boldsymbol{h}^* = \left(\mathbf{0};\,\mathbf{h}^*\right). \tag{10}$$

Remark 1. In the literature, several approaches have been considered to handle the nonlinearity of the rotational equation of motion $(3)_2$. A common formulation exploits that, in a time-continuous framework, $\mathrm{d}\left(\mathbf{J}\boldsymbol{\omega}\right) = \mathbf{J}\mathrm{d}\boldsymbol{\omega} + \boldsymbol{\omega}\times\mathbf{J}\boldsymbol{\omega}\,\mathrm{d}t$, where d stands for the time differential and $\times$ denotes the cross product. Accordingly, in a time-discrete setting, the first term is approximated by $\mathbf{J}\mathrm{d}\boldsymbol{\omega} \approx \mathbf{J}_n\left(\boldsymbol{\omega} - \boldsymbol{\omega}_n\right)$ and the second term is treated in a time-explicit fashion by accounting for the approximate Coriolis and centrifugal forces $\boldsymbol{\omega}_n \times \mathbf{J}_n\,\boldsymbol{\omega}_n$ (e.g., see [72]). A different strategy is adopted here, based on the direct time-discretization $\mathrm{d}\left(\mathbf{J}\boldsymbol{\omega}\right) = \mathbf{J}\boldsymbol{\omega} - \mathbf{J}_n\boldsymbol{\omega}_n$ and on the subsequent linearization of the nonlinear map $\boldsymbol{\omega} \mapsto \mathbf{J}\boldsymbol{\omega}$. On the one hand, such a strategy enables a more accurate treatment of the inertial forces, as it may be required when large angular velocities are involved. On the other hand, numerical experiments show that a single quasi-Newton iteration is generally sufficient for achieving accurate results in the problems under investigation. □

2.2. Unilateral-frictional contacts

The generalized contact impulses $\boldsymbol{\mathcal{I}}$ are determined by the unilateral-frictional contact interactions between the blocks of the system. Actual and potential contacts are established in the given configuration at time t_n, as detailed in Section 3.

The typical contact α is characterized by a pair of antagonist contact points $(P^b)_n^\alpha$ and $(P^{b'})_n^\alpha$, respectively belonging to the blocks b and b', and by a contact direction $\boldsymbol{\nu}_n^\alpha$, e.g. assumed to be oriented from block b to block b' (Fig. 1(a,b)). As a peculiarity of the NSCD formulation, actual and potential contacts are unitarily treated by accounting for the contact interaction whenever the gap between the antagonist contact points:

$$\boldsymbol{g}_n^\alpha = \mathrm{g}_n^\alpha\,\boldsymbol{\nu}_n^\alpha, \quad \mathrm{g}_n^\alpha = \left[(P^{b'})_n^\alpha - (P^b)_n^\alpha\right]\cdot\boldsymbol{\nu}_n^\alpha, \tag{11}$$

is sufficiently small (or, in particular, vanishing). It is here proposed to describe the contact interaction referring to the mid-point between $(P^b)_n^\alpha$ and $(P^{b'})_n^\alpha$, which is denoted by $(M^b)_n^\alpha$ or $(M^{b'})_n^\alpha$ to emphasize whether it is regarded as integral with block b or b',

respectively. Consistently with the configuration update (5), the unilateral-frictional constraints are thus enforced on the contact relative velocity between the points $(M^{b'})^{\alpha}_{n}$ and $(M^{b})^{\alpha}_{n}$ at time t. That is computed by:

$$\boldsymbol{\eta}^{\alpha} = \left[\mathbf{v}^{b'} + \boldsymbol{\omega}^{b'} \times \left((M^{b'})^{\alpha}_{n} - G^{b'}_{n}\right)\right] - \left[\mathbf{v}^{b} + \boldsymbol{\omega}^{b} \times \left((M^{b})^{\alpha}_{n} - G^{b}_{n}\right)\right], \tag{12}$$

where the representation of the rigid-body velocity field of the blocks b and b' is used, and G^{b}_{n} and $G^{b'}_{n}$ are recalled to respectively denote the block centroids at time t_n. The contact relative velocity $\boldsymbol{\eta}^{\alpha}$ can be decomposed into its parallel and orthogonal components with respect to the contact direction:

$$\boldsymbol{\eta}^{\alpha} = \mathrm{w}^{\alpha}\, \boldsymbol{\nu}^{\alpha}_{n} + \mathbf{u}^{\alpha}, \quad \mathrm{w}^{\alpha} = \boldsymbol{\eta}^{\alpha} \cdot \boldsymbol{\nu}^{\alpha}_{n}, \quad \mathbf{u}^{\alpha} = \left(\boldsymbol{I} - \boldsymbol{\nu}^{\alpha}_{n} \otimes \boldsymbol{\nu}^{\alpha}_{n}\right) \boldsymbol{\eta}^{\alpha}, \tag{13}$$

with $\otimes$ denoting tensor product. Corresponding to such contact relative velocity, a work-conjugated contact impulse generally arises, whose parallel and orthogonal components with respect to the contact direction are introduced by:

$$\boldsymbol{\tau}^{\alpha} = \mathrm{n}^{\alpha}\, \boldsymbol{\nu}^{\alpha}_{n} + \mathbf{q}^{\alpha}, \quad \mathrm{n}^{\alpha} = \boldsymbol{\tau}^{\alpha} \cdot \boldsymbol{\nu}^{\alpha}_{n}, \quad \mathbf{q}^{\alpha} = \left(\boldsymbol{I} - \boldsymbol{\nu}^{\alpha}_{n} \otimes \boldsymbol{\nu}^{\alpha}_{n}\right) \boldsymbol{\tau}^{\alpha}. \tag{14}$$

It is observed that, thanks to the choice of enforcing the unilateral-frictional constraints at the mid-point between the antagonist contact points, the internal contact impulses form a self-equilibrated system (Fig. 1(c)). The unilateral-frictional contact interaction is thus translated by the following associative Coulomb constraint conditions [47,65,66,68]:

$$\boldsymbol{\eta}^{\alpha} + \frac{\boldsymbol{g}^{\alpha}_{n}}{\Delta t} \in \left(\mathcal{K}^{\alpha}_{n}\right)^{*}, \quad \boldsymbol{\tau}^{\alpha} \in \mathcal{K}^{\alpha}_{n}, \quad \left(\boldsymbol{\tau}^{\alpha}\right)^{T} \left(\boldsymbol{\eta}^{\alpha} + \frac{\boldsymbol{g}^{\alpha}_{n}}{\Delta t}\right) = 0, \tag{15}$$

in which the superscript ^{T} denotes matrix transposition, whereas the static Coulomb cone $\mathcal{K}^{\alpha}_{n}$ corresponding to a friction coefficient μ and its kinematic polar cone $\left(\mathcal{K}^{\alpha}_{n}\right)^{*}$ are defined by:

$$\mathcal{K}^{\alpha}_{n} = \left\{ \boldsymbol{\tau}^{\alpha} = \mathrm{n}^{\alpha}\, \boldsymbol{\nu}^{\alpha}_{n} + \mathbf{q}^{\alpha} \;\middle|\; \|\mathbf{q}^{\alpha}\| \leq -\mu \mathrm{n}^{\alpha} \right\}, \quad \left(\mathcal{K}^{\alpha}_{n}\right)^{*} = \left\{ \boldsymbol{\eta}^{\alpha} = \mathrm{w}^{\alpha}\, \boldsymbol{\nu}^{\alpha}_{n} + \mathbf{u}^{\alpha} \;\middle|\; \mu \|\mathbf{u}^{\alpha}\| \leq \mathrm{w}^{\alpha} \right\}. \tag{16}$$

It is worth to remark that, consistently with the configuration update (5), the gap g^{α}_{n} enters the constraint conditions (15) for a contact impulse to arise only provided that the two antagonist contact points actually come into contact at time t.

Relationships (15)–(16), which prevail at any contact α, can be compactly written for all the A_n contacts detected on the configuration of the block system at time t_n by introducing the following notation:

$$\boldsymbol{\eta} = \left(\boldsymbol{\eta}^{1}; \ldots; \boldsymbol{\eta}^{A_n}\right), \quad \boldsymbol{\tau} = \left(\boldsymbol{\tau}^{1}; \ldots; \boldsymbol{\tau}^{A_n}\right), \quad \boldsymbol{g}_{n} = \left(\boldsymbol{g}^{1}_{n}; \ldots; \boldsymbol{g}^{A_n}_{n}\right), \quad \mathcal{K}_{n} = \mathcal{K}^{1}_{n} \times \cdots \times \mathcal{K}^{A_n}_{n}, \quad \mathcal{K}^{*}_{n} = \left(\mathcal{K}^{1}_{n}\right)^{*} \times \cdots \times \left(\mathcal{K}^{A_n}_{n}\right)^{*}, \tag{17}$$

and requiring that:

$$\boldsymbol{\eta} + \frac{\boldsymbol{g}_{n}}{\Delta t} \in \mathcal{K}^{*}_{n}, \quad \boldsymbol{\tau} \in \mathcal{K}_{n}, \quad \boldsymbol{\tau}^{T} \left(\boldsymbol{\eta} + \frac{\boldsymbol{g}_{n}}{\Delta t}\right) = 0. \tag{18}$$

The kinematic-static duality finally implies that:

$$\boldsymbol{\eta} = \boldsymbol{D}^{T}_{n} \boldsymbol{v}, \quad \boldsymbol{\mathcal{I}} = -\boldsymbol{D}_{n} \boldsymbol{\tau}, \tag{19}$$

with $\boldsymbol{D}_{n}$ as a suitable static-kinematic operator, whose definition is e.g. inferred by the kinematic relationships (12)–(13). Accordingly, the generalized contact impulses $\boldsymbol{\mathcal{I}}$ are obtained, work-conjugated with the generalized velocities $\boldsymbol{v}$ and to be accounted for in the equations of motion (8).

Remark 2. It is pointed out that, in the imposition of the unilateral-frictional constraints between the blocks of the system, the treatment of the system configuration is time-explicit because, as previously noticed, the pairs of antagonist contact points and the relevant contact directions are evaluated at time t_n. The typical contact relative velocity $\boldsymbol{\eta}^{\alpha}$ at time t is derived from Eq. (12) using the linear and angular velocities of the blocks at time t, with the relative position vectors of the contact points from the relevant block centroids computed at time t_n. Such a time-explicit configuration treatment in the imposition of contact constraints only partially restricts the possibility of adopting large time steps of integration within the proposed NSCD formulation, as allowed from the method to be time-implicit in all other aspects. □

2.3. Variational formulation

Relationships (8), (18), and (19) govern the dynamic evolution of the block system under the prescribed external forces. Such a problem can be regarded as the set of stationarity conditions of the following mixed variational formulation:

$$\max_{\boldsymbol{\tau} \in \mathcal{K}_{n}} \min_{\boldsymbol{v}} \quad \left\{ \frac{1}{2} \left(\boldsymbol{v} - \boldsymbol{v}_{n}\right)^{T} \boldsymbol{H}^{*} \left(\boldsymbol{v} - \boldsymbol{v}_{n}\right) - \left(\boldsymbol{v} - \boldsymbol{v}_{n}\right)^{T} \left(\boldsymbol{b}\, \Delta t + \boldsymbol{h}^{*}\right) + \boldsymbol{\tau}^{T} \left(\boldsymbol{D}^{T}_{n} \boldsymbol{v} + \frac{\boldsymbol{g}_{n}}{\Delta t}\right) \right\}. \tag{20}$$

By a-priori enforcing the stationarity conditions with respect to the static variables, i.e. the contact impulses $\boldsymbol{\tau}$, a kinematic variational formulation is obtained:

$$\begin{aligned} &\min_{\boldsymbol{v}} \quad \left\{ \frac{1}{2} \left(\boldsymbol{v} - \boldsymbol{v}_{n}\right)^{T} \boldsymbol{H}^{*} \left(\boldsymbol{v} - \boldsymbol{v}_{n}\right) - \left(\boldsymbol{v} - \boldsymbol{v}_{n}\right)^{T} \left(\boldsymbol{b}\, \Delta t + \boldsymbol{h}^{*}\right) \right\} \\ &\text{s.t.} \quad \boldsymbol{\eta} = \boldsymbol{D}^{T}_{n} \boldsymbol{v}, \quad \boldsymbol{\eta} + \frac{\boldsymbol{g}_{n}}{\Delta t} \in \mathcal{K}^{*}_{n}, \end{aligned} \tag{21}$$

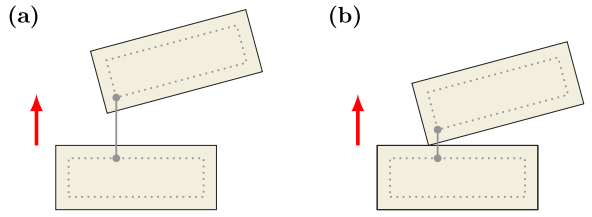

Fig. 2. Collision detection: contact direction between two blocks, determined as the direction of minimum distance of shrunken copies of the two blocks, in case of blocks that are (a) well-separated or (b) in contact.

consisting in a second-order conic programming (SOCP) problem. When addressing its solution, the final velocity $\boldsymbol{v}$ is directly obtained as the primary variable. On the other hand, the dual variables are recovered from the Karush–Kuhn–Tuckers (KKT) multipliers associated with kinematic conic constraints, recognized to be the contact impulses $\boldsymbol{\tau}$. In a similar fashion, by a-priori enforcing the stationarity conditions with respect to the final velocity $\boldsymbol{v}$, a static variational formulation descends from the mixed problem (20), reading:

$$\begin{aligned} \max_{\boldsymbol{\tau}} \quad & \left\{ -\frac{1}{2}\boldsymbol{p}^T \left(\boldsymbol{H}^*\right)^{-1}\boldsymbol{p} + \boldsymbol{\tau}^T \left(\boldsymbol{D}_n^T \boldsymbol{v}_n + \frac{\boldsymbol{g}_n}{\Delta t} \right) \right\} \\ \text{s.t.} \quad & \boldsymbol{p} = \boldsymbol{\mathcal{I}} + \boldsymbol{b}\Delta t + \boldsymbol{h}^*, \quad \boldsymbol{\mathcal{I}} = -\boldsymbol{D}_n \boldsymbol{\tau}, \quad \boldsymbol{\tau} \in \mathcal{K}_n, \end{aligned} \tag{22}$$

which represents the dual SOCP problem of the one in Eq. (21). Specifically, $\boldsymbol{p}$ is interpreted as the vector of generalized resultant impulses acting on the system blocks, work-conjugated with the generalized velocities $\boldsymbol{v}$ and contributed from both generalized external and contact impulses. Moreover, the generalized velocity update $\boldsymbol{v} - \boldsymbol{v}_n$ is computed as $(\boldsymbol{H}^*)^{-1}\boldsymbol{p}$.

Remark 3. It is emphasized that the choice to adopt the quasi-Newton scheme (6) for the solution of the nonlinear rotational equation of motion $(3)_2$, with $\mathbf{H}^*$ as the positive semidefinite part of the Jacobian of the nonlinear map $\boldsymbol{\omega} \mapsto \mathbf{J}\boldsymbol{\omega}$, is instrumental for problems (21) and (22) to be SOCPs. Accordingly, they can be addressed by highly-efficient convex optimization software available in the literature [83]. Should a full Newton method be adopted instead, a variational formulation would not be generally available for problem (8), (18), and (19), for the Jacobian is not guaranteed to be symmetric. On the other hand, a quasi-Newton scheme adopting the symmetric part of the Jacobian might result in a nonconvex optimization problem. □

Remark 4. As a consequence of the rigid body idealization of the system blocks, the kinematic and static formulations (21) and (22) may admit multiple solutions in terms of contact impulses when statically indeterminate structures are considered. In order to avoid such a multiplicity of solutions, in [72], it has been proposed to resort to a numerical compliance as a regularization. Nonetheless, the assumption that rigid bodies have infinite strength [1–3], together with the admissibility conditions $(18)_2$ on contact impulses, guarantees the equivalence of those solutions. □

Remark 5. In [65], it has been shown that the velocity history obtained in solution of the time-discrete problem (8), (18), and (19) converges, for vanishing time step Δt, to the solution of the time-continuous dynamic problem assuming unilateral-frictional contacts with non-associative Coulomb frictional behavior and zero dilatancy. As expected, the limit velocity is a function of bounded variation characterized by jump discontinuities due to the contacts between the blocks, and the convergence of the numerical discrete scheme is intended as a weak* convergence of measures. □

3. Collision detection

In order to impose the unilateral-frictional constraints discussed in the previous section, the actual and potential contacts between the blocks of the system need to be computed in the typical structural configuration. Such a task is performed by means of a collision detection algorithm, which is here presented. The algorithm assumes that each block is a convex polyhedron (non-convex polyhedral blocks could still be considered, as represented as the union of convex polyhedral sub-blocks, rigidly constrained with each other by standard kinematic constraints in the form of linear equality conditions on the block velocities). As suggested in [72], for numerical efficiency, the algorithm is split into a broad and a narrow phase to be performed sequentially. In the broad phase, the pairs of blocks close enough to be in actual or potential contact are identified by a bounding box technique. Next, each pair of interacting blocks is considered in the narrow phase to determine relevant pairs of antagonist contact points between the blocks.

As a model assumption, it is here postulated that a single contact direction characterizes all possible pairs of antagonist contact points between two interacting blocks. Such a contact direction is determined by resorting to the Gilbert-Johnson-Keerthi (GJK) algorithm [86,87], which returns a pair of nearest points between any pair of given convex shapes. Direct use of the GJK algorithm on two interacting blocks is not advisable because it would result in coincident nearest points for convex shapes that are not well-separated. Indeed, interacting blocks may not be well-separated either because they are in actual contact with each other or because they are even slightly interpenetrating due to numerical inaccuracies accumulated during the simulation. As an expedient proposed in [72], the GJK algorithm is performed on shrunken copies of the blocks, with the shrinking factor to be calibrated as a geometrical

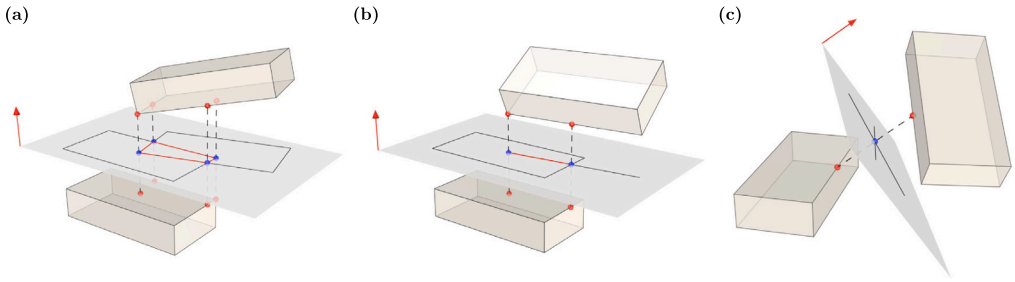

Fig. 3. Collision detection: potential contacts between two blocks along a prescribed contact direction in case of (a) face-to-face, (b) edge-to-face, or (c) edge-to-edge interactions. Antagonist contact points are depicted in red. They are obtained by projecting the visible faces of the blocks onto the orthogonal plane to the contact direction, by considering the intersection convex polygon of the projected faces (in red), and by projecting back onto the blocks the vertices (in blue) of the intersection convex polygon. Pairs of antagonist contact points too far apart from each other are discarded (and not shown). (For interpretation of the references to color in this figure legend, the reader is referred to the web version of this article.)

Table 1
Numerical results: friction coefficient μ adopted in time-history analyses at the interfaces between the blocks and between the blocks and the foundation.

Numerical problem	Friction coefficient μ	
	Block-to-block	Block-to-foundation
Housner block	–	2
Single 3D rigid block	–	2
Multi-block arch	2	2
Spandrel arch	0.4	0.4
Stone house	0.7	0.9
Historical church	0.6	0.6

tolerance of the problem (Fig. 2). The contact direction between the interacting blocks is therefore selected as the direction of minimum distance between their shrunken copies, provided that such a distance is small enough (otherwise, the pair of interacting blocks is discarded from potential contacts).

Once the contact direction is found, relevant pairs of antagonist contact points must be determined between the two interacting blocks. To that aim, a visibility check is performed on the faces of the two blocks by restricting the attention to those faces whose outer normal vector forms an acute angle with the contact direction (as oriented from the block under consideration to the interacting one). The visible faces of the two blocks are then projected onto the orthogonal plane to the contact direction, resulting in a set of convex polygons. The intersection of every convex polygon that descends from the visible faces of one block is considered with every convex polygon that descends from the visible faces of the other block. A pair of antagonist contact points between the interacting blocks is determined by projecting back, onto the blocks along the contact direction, the vertices of each non-void intersection convex polygon. Finally, possible duplicated pairs of antagonist contact points or pairs of antagonist contact points that are too far apart from each other are discarded.

It is worth observing that the procedure above is capable to automatically determine the antagonist contact points between two interacting blocks irrespective of their participation into the contact through one of their faces, edges or vertices. For an illustration, Fig. 3 shows the pairs of antagonist contact points resulting in case of (a) face-to-face, (b) edge-to-face, or (c) edge-to-edge interactions. Finally, unilateral-frictional constraints are enforced for each detected pair of antagonist contact points, as previously discussed in Section 2.2.

Remark 6. It is noticed that the present modeling assumption to consider a single contact direction for all the pairs of antagonist contact points between two interacting blocks is in line with a similar assumption in the DEM software 3DEC®. In that case, a common-plane is introduced for two interacting blocks, defined as the plane separating them and maximizing the gap from the closest vertex (in practice, the maximization problem is only approximatively solved) [88]. The normal unit vector to such a common-plane is the contact direction between the blocks, here derived by the GJK algorithm as the direction of minimum distance between the shrunken copies of the two blocks (for alternative collision detection algorithms developed within DEM, see [89]). Conversely, in [72], the pair of nearest points returned by the GJK algorithm defines both a pair of antagonist contact points and the contact direction between them. Additional pairs of antagonist contact points are then detected by repeating the procedure with small rotational perturbations of the configuration of the blocks. As a result, the contact direction may therein be slightly different for different pairs of antagonist contact points of two interacting blocks. □

4. Numerical results

In this section, numerical simulations are presented for exploring the capabilities of the proposed variational NSCD formulation in predicting the dynamic behavior of block masonry structures subject to ground excitation. Specifically, three benchmark problems

Table 2
Numerical results: number of blocks B, time step Δt, and average CPU time per time step taken in time-history analyses to perform the collision detection (broad and narrow phases are separately considered) and to solve the time-step optimization problem. Times are expressed in s.

Numerical problem	No. blocks B	Time step Δt	Average CPU time per time step		
			Collision detection		Optimization
			Broad	Narrow	
Housner block	1	0.001	0.00002	0.0002	0.004
Single 3D rigid block	1	0.001	0.00002	0.0002	0.008
Multi-block arch	7	0.001	0.00007	0.002	0.01
Spandrel arch	201	0.001	0.002	0.07	0.1
Stone house	191	0.001	0.002	0.06	0.4
Historical church	5161	0.002	0.3	2.2	9.5

dealing with time-history analyses of the Housner block (Section 4.1), of a 3D rigid block (Section 4.2), and of a multi-block masonry arch (Section 4.3) are addressed for a validation. Then, a spandrel arch (Section 4.4), a stone house (Section 4.5), and a historic church (Section 4.6) are investigated as full-scale structural applications, enlightening their dynamic response and failure domains.

All numerical analyses have been performed using an in-house MATLAB®code, and the computations have been done on a single machine with dual Intel® Xeon® CPU Gold 6226R @ 2.89 GHz and 256 GB RAM. Mosek® optimization software (version 10.1) [83] has been adopted to solve the time-step optimization problem. In particular, it has been observed that the kinematic and static formulations (21) and (22), respectively, provide identical results, with the implementation of the kinematic formulation being computationally more efficient.

Table 1 reports the friction coefficient μ adopted in the time-history analyses at the interfaces between the blocks and between the blocks and the foundation (the large value $\mu = 2$ is chosen to numerically match a no-sliding condition). Moreover, Table 2 summarizes the number of blocks B, the time step Δt, and the average CPU times per time step taken in the time-history analyses to perform the collision detection (broad and narrow phases are separately considered) and to solve the time-step optimization problem. It is noticed that the former CPU times could be improved by optimizing the programming of the collision detection algorithm, whereas the latter time is fully ascribable to Mosek® optimization software.

4.1. Housner block

The classical Housner problem dealing with the free rocking motion of a 2D rigid block [4] is investigated for a first basic validation of the proposed variational NSCD formulation. The block, of rectangular shape with a basis of $2b$ and a height of $2h$, has uniform mass density and is supported on a rigid plane where a no-sliding condition is assumed. The block is initially tilted with respect to the vertical by an angle ϑ_0. In time-history analyses, the following parameters are considered: $b = 0.30\,\mathrm{m}$, $h = 1\,\mathrm{m}$, $\vartheta_0 = 15°$.

A benchmark event-driven solution for the free rocking motion is obtained from the numerical integration of the following equation of motion [12]:

$$\ddot{\vartheta}(t) = -p^2 \sin\left[\alpha \operatorname{sgn}\vartheta(t) - \vartheta(t)\right], \quad \vartheta(0) = \vartheta_0, \quad \dot{\vartheta}(0) = 0, \tag{23}$$

where ϑ is the block rotation angle with respect to the vertical, $\alpha = \tan^{-1}(b/h)$ is the block slenderness angle, $p = \sqrt{3g/(4R)}$ is the block frequency parameter depending on the radius $R = \sqrt{b^2 + h^2}$, and sgn denotes the sign function. The numerical integration was performed in MATLAB® using the built-in function ode23, which implements a Runge–Kutta integration scheme and allows for a treatment of the events. At any event, detected as a zero-crossing of the rotation angle and thus corresponding to an impact of the block against the supporting plane, the rotation angle is kept fixed, and the block velocity (after the impact) is set to the block velocity before the impact times the Housner angular-velocity coefficient of restitution $r = [1 + 3\cos(2\alpha)]/4$ [4].

Fig. 4(a) shows the solution obtained by the proposed formulation in the phase plane, with $\omega(t) = \dot{\vartheta}(t)$ denoting the block angular velocity. In order to enlighten the convergence properties of the method, the decreasing values $\Delta t = \{0.001, 0.0005, 0.0001\}$ s of the time step are considered. It is noticed that numerical results are already at convergence for the largest analyzed time step $\Delta t = 0.001$ s. In Fig. 4(b), the (converged) time history of the total, kinetic, and potential energy per unit weight is given. Sudden drops in the kinetic energy are observed at the impacts of the block against the supporting plane, consistently with the time history of the dissipated energy per unit weight. Interestingly, no significant algorithmic energy dissipation can be noticed. The obtained numerical results are in very good agreement with the benchmark ones reported as black dashed lines. Consequently, those results provide a validation of the present formulation and confirm its consistency with the classical Housner impact model.

Remark 7. Some control on the coefficient of restitution could be achieved within the present formulation by extending the approach proposed in [90] to the NSCD setting. The basic idea is to assume that the block basis is not perfectly plane but presents one or more small bumps. Consequently, the typical impact against the supporting plane occurs in several consecutive time steps. Numerical results show that such an approach accomplishes an increase in the coefficient of restitution and is thus capable of overcoming possible overestimation of the kinetic energy dissipation by Housner's model. □

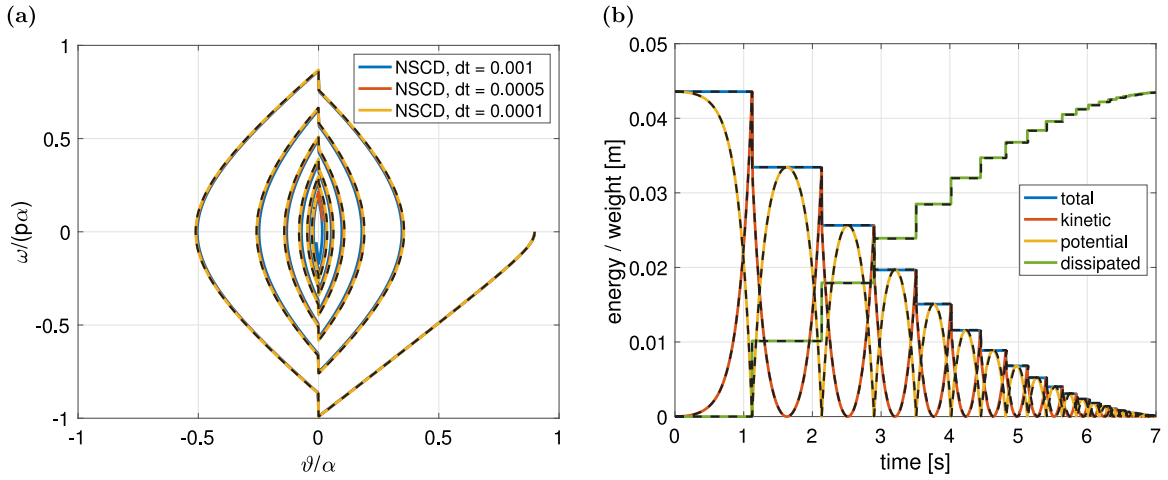

Fig. 4. Housner block: (a) phase portrait and (b) time history of energy per unit weight in free rocking motion. Reference results, obtained by numerical integration of the equation of motion (23) by MATLAB® built-in function ode23, are reported for comparison as black dashed lines. (For interpretation of the references to color in this figure legend, the reader is referred to the web version of this article.)

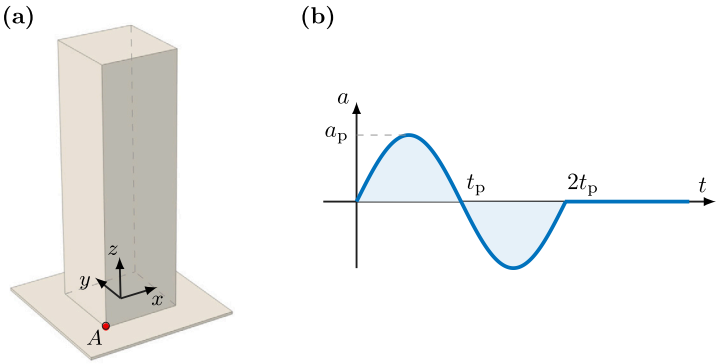

Fig. 5. Single 3D rigid block: (a) geometric model and (b) one-sine impulse ground acceleration.

4.2. Single 3D rigid block

As a 3D benchmark problem for the proposed variational NSCD formulation, the case study discussed in [36] of a parallelepiped rigid block subject to pulse-type excitation is considered. The block is assumed to be characterized by a squared basis with a side length of $2b$ and a height of $2h$, and to have a uniform mass density (Fig. 5a). A no-sliding condition is assumed to hold between the basis of the block and the ground. Upon introducing a Cartesian reference frame $(O; x, y, z)$ with origin O at the basis centroid and coordinate axes parallel to the block edges, a one-sine impulse ground acceleration of amplitude a_p and half-period t_p is applied to the block (Fig. 5b) along the horizontal direction forming an angle α with the x-axis. Time history analyses are performed by setting $b = 0.30\,\mathrm{m}$, $h = 1\,\mathrm{m}$, and $\alpha = 44°$.

The application of a one-sine impulse with $a_\mathrm{p} = 8\,\mathrm{m/s^2}$ and $t_\mathrm{p} = 0.25\,\mathrm{s}$ is initially investigated. In Fig. 6(a), an account of the predicted block motion is delivered by the time history of the z-displacement of the point $A \equiv (-b, -b, 0)$. In order to investigate the convergence properties of the proposed formulation, numerical results obtained for the values $\Delta t = \{0.001, 0.0005, 0.0001\}\,\mathrm{s}$ of the time step are shown. The numerical results obtained for the finest investigated time step $\Delta t = 0.0001\,\mathrm{s}$ are at convergence and in excellent agreement with the reference solution (black dashed line) computed in [36] by adopting an event-driven approach and the classical Housner impact model. Nonetheless, it is remarked that satisfactory accuracy is already achieved, from an engineering perspective, for the coarsest investigated time step $\Delta t = 0.001\,\mathrm{s}$.

An interpretation of the overall dynamic response of the block is favored by supplementing the displacement time history in Fig. 6(a) with the energy time history shown in Fig. 6(b). In addition to the (converged) time history of the total, kinetic, and potential energy per unit weight, harvested and dissipated energy per unit weight are reported, respectively computed as the cumulative work done by the external forces per unit weight and as the difference between the harvested and total energy per unit weight. It emerges that the block undergoes a 3D rocking motion in which several consecutive impacts dissipate its total energy until it comes to rest. A glimpse of such a rocking motion is delivered by Fig. 7, which shows the block configurations at the time

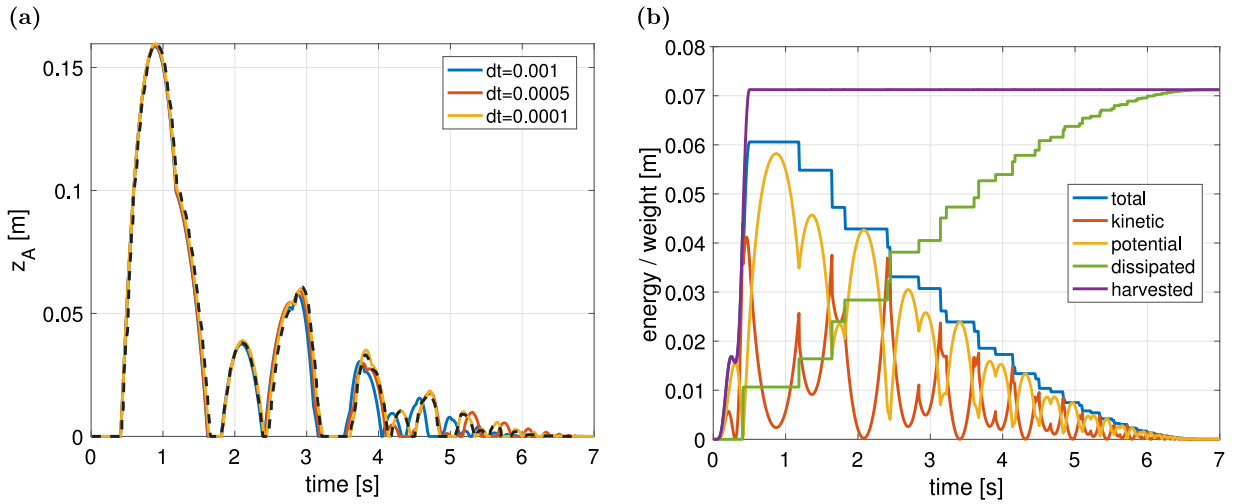

Fig. 6. Single 3D rigid block: time history of (a) z-displacement of basis vertex A and (b) energy per unit weight, in response to a one-sine impulse of amplitude $a_p = 8\,\mathrm{m/s^2}$ and half-period $t_p = 0.25\,\mathrm{s}$ along the horizontal direction forming an angle $\alpha = 44°$ with respect to the x-axis. Reference results [36] are reported for comparison as black dashed line. (For interpretation of the references to color in this figure legend, the reader is referred to the web version of this article.)

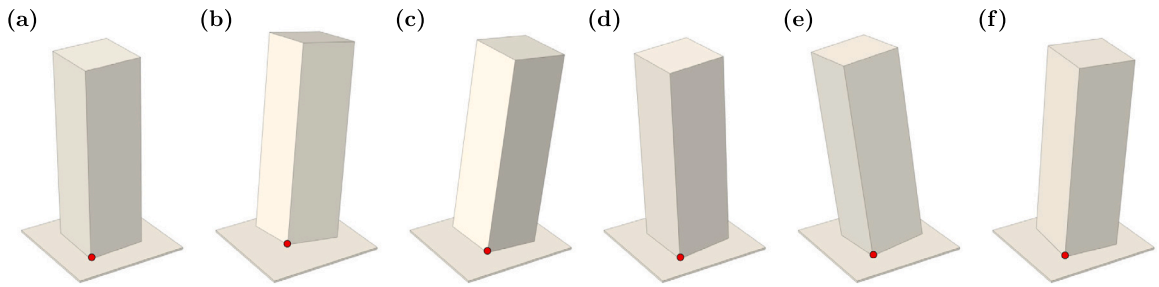

Fig. 7. Single 3D rigid block: deformed configuration attained at potential-energy peaks at time instants (a)–(f) $t = \{0.3, 0.85, 1.35, 1.75, 2.1, 2.7\}$ s, in response to a one-sine impulse of amplitude $a_p = 8\,\mathrm{m/s^2}$ and half-period $t_p = 0.25\,\mathrm{s}$ along the horizontal direction forming an angle $\alpha = 44°$ with respect to the x-axis. The red marker identifies point A. (For interpretation of the references to color in this figure legend, the reader is referred to the web version of this article.)

instants $t = \{0.3, 0.85, 1.35, 1.75, 2.1, 2.7\}$ s approximately coinciding with the first six potential-energy peaks. It is found that the block starts rotating about vertex A during the first half-sine impulse and, after a first major impact, continues rotating about the diagonally opposite vertex during the second half-sine impulse. Subsequently, a free rocking motion occurs, characterized by block oscillations alternately about all the basis vertices and with progressively higher frequency, which extends up to a complete decay of the block total energy.

The effect of a stronger ground acceleration is next considered by selecting the amplitude $a_p = 9.5\,\mathrm{m/s^2}$ for the one-sine impulse while leaving its half-period $t_p = 0.25\,\mathrm{s}$ unchanged. The obtained numerical results are shown in Fig. 8, adopting the same format as introduced above. From panel (a), the convergence properties of the present approach with respect to the time step are substantially confirmed, and a satisfactory agreement is found with the benchmark solution (black dashed line) from [36]. From also inspecting panel (b), it is observed that, despite an initial rocking motion of the block partially dissipating its total energy, the increased acceleration amplitude eventually implies its collapse. That is proven by the final and simultaneous diverging of the z-displacement of point A and of the kinetic and potential energy of the block. The block configurations at the time instants $t = \{0.3, 0.95, 1.6, 2.15, 2.15\}$ s approximately coinciding with the potential-energy peaks, and at the time instant $t = 2.7\,\mathrm{s}$ are shown in Fig. 9.

In closing, the present numerical results provide a validation of the proposed variational NSCD formulation in predicting the complex 3D rocking motion of a block subject to pulse-type ground excitation. The very good comparison with results from an event-driven approach based on the Housner impact model emphasizes the mechanical merit of the formulation and the numerical efficiency achieved by avoiding refined time-detection of impacts.

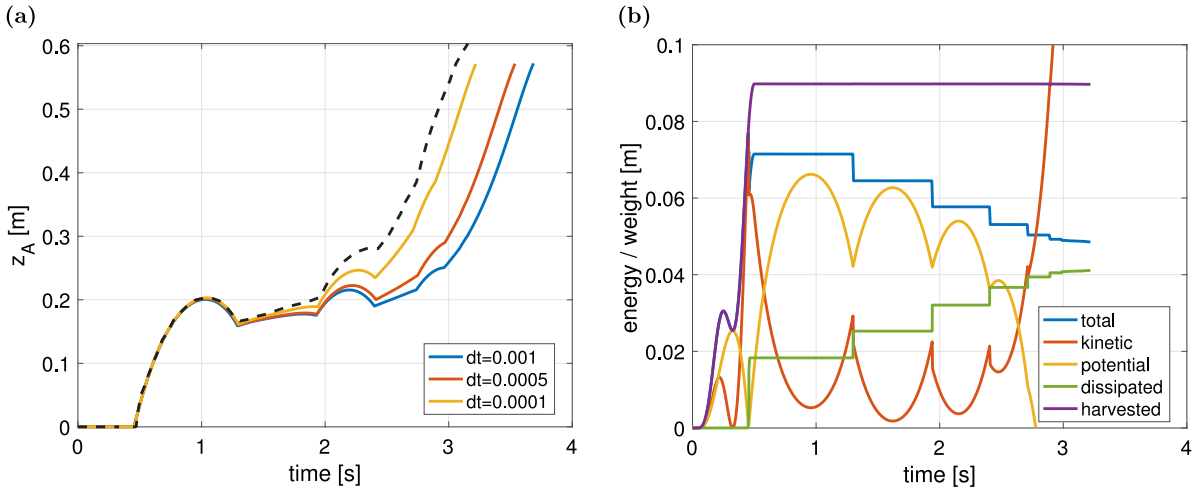

Fig. 8. Single 3D rigid block: time history of (a) z-displacement of base vertex A and (b) energy per unit weight, in response to a one-sine impulse of amplitude $a_p = 9.5\,\mathrm{m/s^2}$ and half-period $t_p = 0.25\,\mathrm{s}$ along the horizontal direction forming an angle $\alpha = 44°$ with respect to the x-axis. Reference results [36] are reported for comparison as black dashed line. (For interpretation of the references to color in this figure legend, the reader is referred to the web version of this article.)

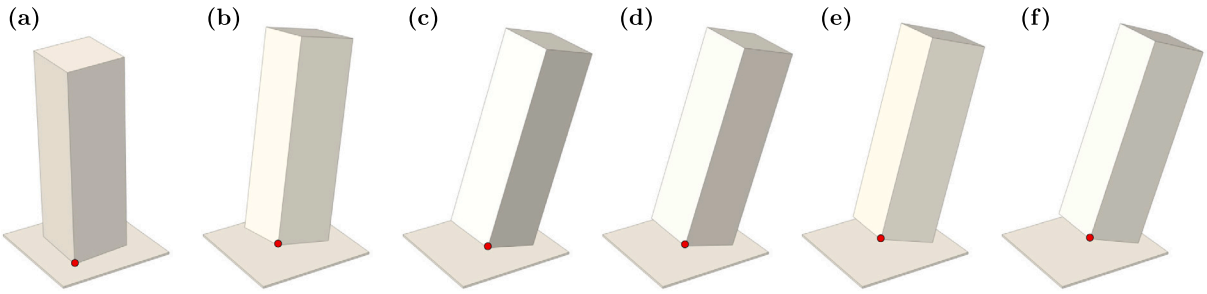

Fig. 9. Single 3D rigid block: deformed configuration attained at potential-energy peaks at time instants (a)–(e) $t = \{0.3, 0.95, 1.6, 2.15, 2.5\}$ s, and at incipient collapse at time instant (f) $t = 2.7\,\mathrm{s}$, in response to a one-sine impulse of amplitude $a_p = 9.5\,\mathrm{m/s^2}$ and half-period $t_p = 0.25\,\mathrm{s}$ along the horizontal direction forming an angle $\alpha = 44°$ with respect to the x-axis. The red marker identifies point A. (For interpretation of the references to color in this figure legend, the reader is referred to the web version of this article.)

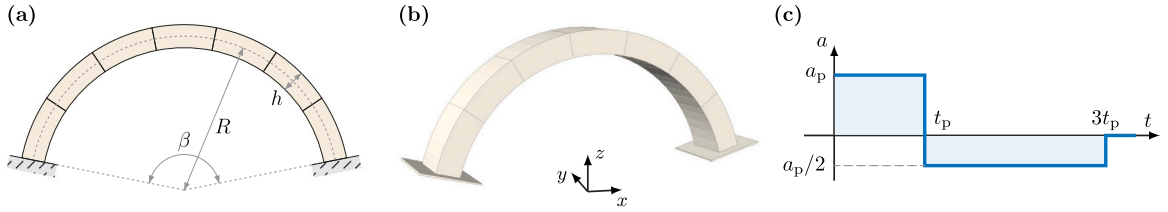

Fig. 10. Multi-block arch: (a) geometric model, (b) perspective view of the adopted numerical model, and (c) biphasic impulse ground acceleration.

4.3. Multi-block arch

For a further validation of the proposed variational NSCD formulation, the problem of a multi-brick arch known as Oppenheim's arch [22] undergoing an in-plane pulse-type excitation is investigated. The arch is characterized by a circular mid-curve of radius $R = 10\,\mathrm{m}$, thickness-over-radius ratio h/R, and embrace angle β (Fig. 10(a,b)). A no-sliding condition is assumed to hold between the $B = 7$ blocks and between the blocks and the ground. The arch is subjected to a biphasic impulse ground acceleration, i.e. to a pulse of constant acceleration a_p for a duration t_p, followed by a pulse of constant acceleration $a_p/2$ in the opposite direction for a duration $2t_p$ (Fig. 10c) acting within the arch plane (the first acceleration pulse is assumed leftwards).

As in proposed in [34], a time-history analysis of the Oppenheim arch is performed in the case $h/R = 0.15$ and $\beta = 150°$. The values $a_p = 1.11\,g$, with g as the gravity acceleration, and $t_p = 0.30\,\mathrm{s}$ are selected for the applied biphasic impulse (the

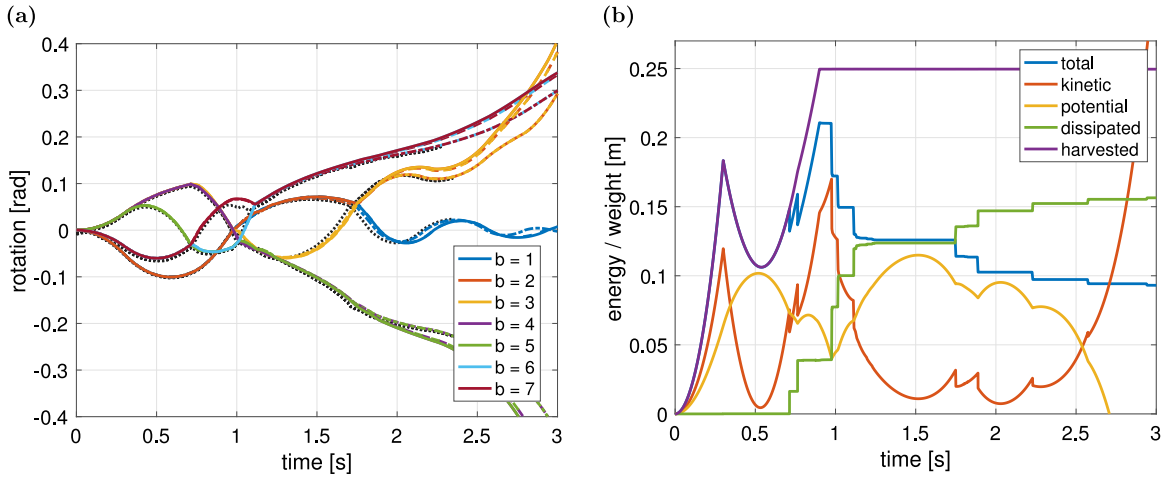

Fig. 11. Multi-block arch: time history of (a) block rotations and (b) energy per unit weight, for a circular arch with radius $R = 10\,\mathrm{m}$, normalized thickness $h/R = 0.15$, and embrace angle $\beta = 150°$, in response to an in-plane biphasic impulse of amplitude $a_\mathrm{p} = 1.11\,\mathrm{g}$ and duration $t_\mathrm{p} = 0.30\,\mathrm{s}$. The blocks are numbered from right to left. Numerical results at varying of the time step $\Delta t = \{0.001, 0.0005, 0.0001\}$ s are reported as dash-dotted, dashed, and solid lines, respectively. Reference results [34] are reported for comparison as black dotted line. (For interpretation of the references to color in this figure legend, the reader is referred to the web version of this article.)

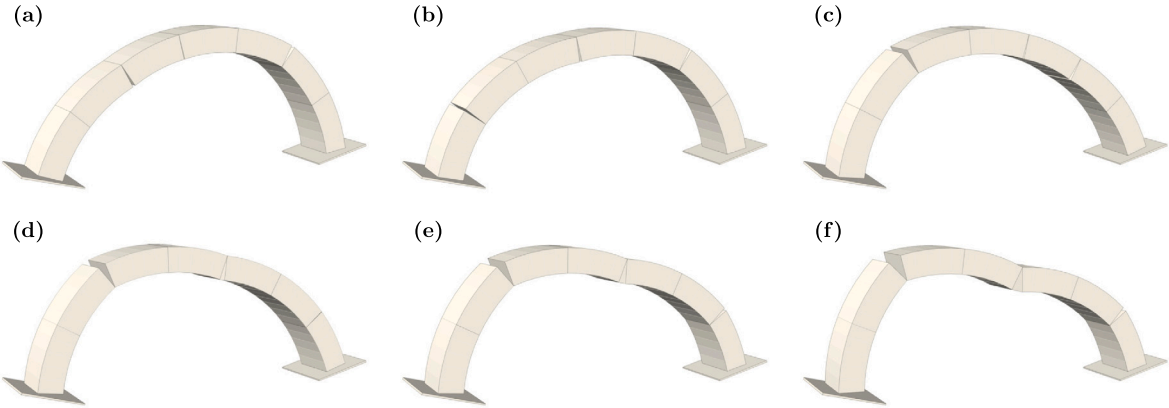

Fig. 12. Multi-block arch: deformed configuration attained at potential-energy peaks at time instants (a)–(e) $t = \{0.5, 0.85, 1.5, 1.75, 2\}$ s, and at incipient collapse at time instant (f) $t = 2.5\,\mathrm{s}$, for a circular arch with radius $R = 10\,\mathrm{m}$, normalized thickness $h/R = 0.15$, and embrace angle $\beta = 150°$, in response to an in-plane biphasic impulse of amplitude $a_\mathrm{p} = 1.11\,\mathrm{g}$ and duration $t_\mathrm{p} = 0.30\,\mathrm{s}$.

pseudo-static seismic capacity of the arch, as determined by standard limit analysis, is of $0.444g$). In Fig. 11(a), the time history predicted for the rotation angles of the blocks (as numbered from right to left) is depicted. Numerical results at varying of the time step $\Delta t = \{0.001, 0.0005, 0.0001\}$ s are reported as dash-dotted, dashed, and solid lines, respectively. They confirm the convergence properties of the present formulation and are found to be in very good agreement with the reference solution (black dotted line) computed in [34] by an event-driven approach based on the classical Housner impact model. Fig. 11(b) shows the (converged) time history of total, kinetic, potential, dissipated and harvested energy per unit weight.

As a qualitative description, it is observed that the arch motion (towards the right) initiates along the pseudo-static four-hinge mechanism, with a peak of the kinetic energy attained at the end of the first pulse. While the arch recovers from such first excitation, the inversion of the arch motion during the return pulse triggers a rocking motion. Several impacts take place, which produce sudden drops in the kinetic energy of the system and, through the subsequent closing and opening of diverse hinges, imply a complex motion. Despite the energy dissipation due to impacts, the arch collapses (moving towards the left). That is proven by the final and simultaneous diverging of the rotation angles of all the blocks (except for the first one, which eventually returns to rest) and of the kinetic and potential energy. The arch configurations at the time instants $t = \{0.5, 0.85, 1.5, 1.75, 2\}$ s approximately coinciding with the potential-energy peaks, and at the time instant $t = 2.7\,\mathrm{s}$ are shown in Fig. 12, highlighting the fast evolution of the hinge locations during the rocking of the arch.

As a concluding remark, the present numerical results validate the capabilities of the proposed variational NSCD formulation also in addressing the dynamic response of a multi-block arch under in-plane ground excitation. Compared to the single-rigid-block

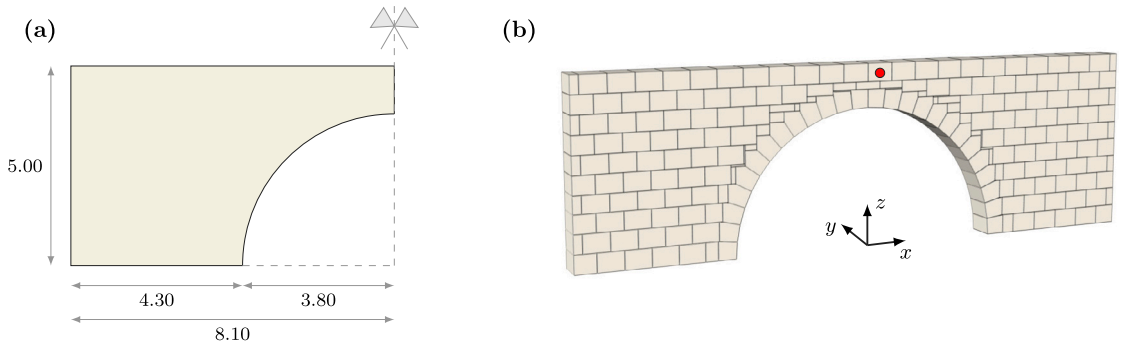

Fig. 13. Spandrel arch: (a) geometric model, with dimensions expressed in m, and (b) perspective view of the adopted numerical model [72].

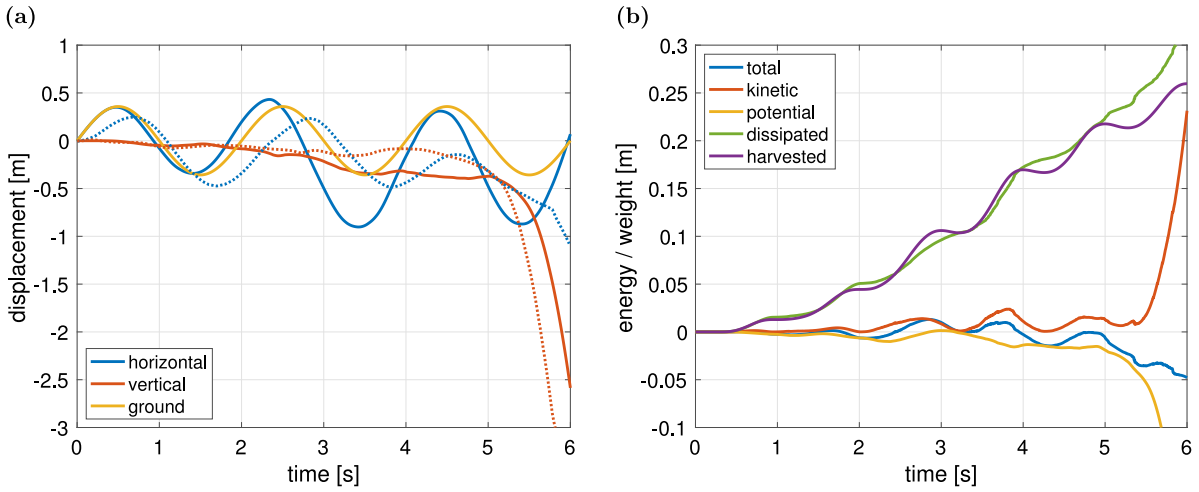

Fig. 14. Spandrel arch: time history of (a) monitored block and (b) energy per unit weight, in response to an in-plane sinusoidal acceleration of amplitude $a_p = 0.36\,g$ and half-period $t_p = 1\,s$. Reference results [72] are reported for comparison as dotted line. (For interpretation of the references to color in this figure legend, the reader is referred to the web version of this article.)

problem, the interaction between multiple blocks is automatically accounted for by the implemented collision detection algorithm, which accurately predicts the non-trivial sequence of opening and closing hinges. Finally, the consistency of the formulation with the Housner impact model is further verified.

4.4. Spandrel arch

In this section, the dynamic behavior of the spandrel arch shown in Fig. 13 is considered to test the performances of the proposed NSCD formulation in a full-scale structural application. Such a case study is inspired by a similar problem addressed in [72], where the wall is specified to be $H = 5\,m$ high, $t = 0.8\,m$ thick, $L = 16.2\,m$ long, and the arch inner radius is given as $R = 3.8\,m$. In order to mimic the rounding and smoothing of the block corners therein adopted, a trimming procedure is implemented here to chip the block edges. Specifically, for $\boldsymbol{v}_1$ and $\boldsymbol{v}_2$ denoting unit vectors normal to the two block faces that share the typical edge, the block is trimmed by a plane at distance εH from the exterior support plane to the block whose normal vector is parallel to $\boldsymbol{v}_1 + \boldsymbol{v}_2$. In numerical simulations, it is set $\varepsilon = 0.0015$. The structure comprises $B = 201$ blocks, which are assumed of uniform mass density. A Cartesian reference frame $(O; x, y, z)$ is introduced, such that the x- and z-axes define the in-plane horizontal and vertical direction, respectively, and the y-axis defines the out-of-plane direction. A sinusoidal ground motion is applied along the x-direction, such that the corresponding ground acceleration is of amplitude $a_p = 0.36\,g$ and half-period $t_p = 1\,s$ (the first acceleration pulse is assumed leftwards). Based on the evidence from the convergence analysis carried out in the three benchmark problems previously discussed, the time step $\Delta t = 0.001\,s$ has been adopted in numerical simulations, which conjugates numerical accuracy and computational efficiency.

Fig. 14(a) shows the time history numerically predicted for the in-plane horizontal and vertical displacements of the block centroid indicated by a marker in Fig. 14(b), given the applied ground displacement time history. For comparison, results from [72] are reported as dashed lines, implying a reasonable qualitative agreement (observed differences are mainly ascribable to not-perfectly

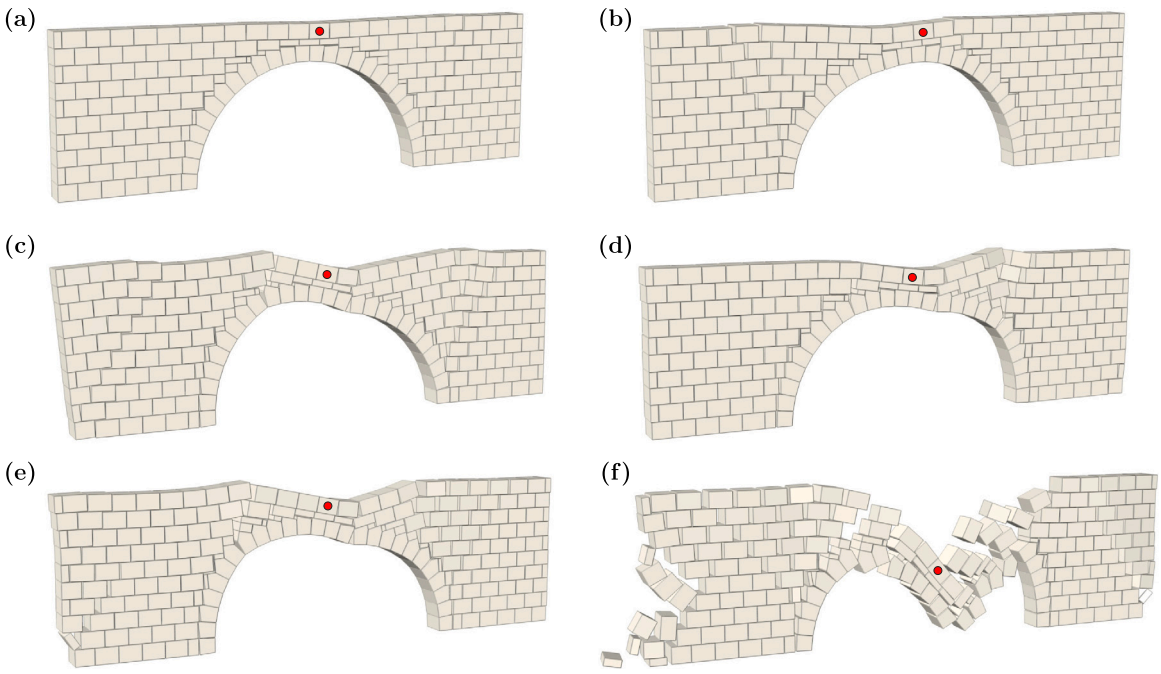

Fig. 15. Spandrel arch: deformed configuration attained at time instants (a)–(f) $t = \{1, 2, 3, 4, 5, 6\}$ s, in response to an in-plane sinusoidal acceleration of amplitude $a_p = 0.36\,g$ and half-period $t_p = 1$ s. The red marker identifies the monitored block. (For interpretation of the references to color in this figure legend, the reader is referred to the web version of this article.)

matching geometric models). Fig. 14(b) illustrates the time history of total, kinetic, potential, dissipated, and harvested energy per unit weight.

It is observed that the horizontal displacement of the monitored block centroid coincides with the ground displacement until the impulse ground acceleration reaches the pseudo-static seismic capacity of the spandrel arch, determined by a standard limit analysis, of 0.284 g. Subsequently, the relative motion of the structure with respect to the ground initiates. It is characterized by a sequence of oscillations in the horizontal direction exhibiting a phase lead compared to the ground motion. The structural configurations attained at the time instants $t = \{1, 2, 3, 4, 5, 6\}$ s are depicted in Fig. 15, showing the progressive disassembling and damaging process of the structure until its final collapse. The structural motion is significantly influenced by shear sliding occurring in the spandrels, as enabled by the limited available friction coefficient. In particular, the sliding at the base of the spandrels induces springing settlements of the arch, which thus enter a hinge mechanism. In the initial stages of the motion, panels (a)–(c), the structural motion follows the alternating direction of the ground motion, with diagonal shear cracks in the spandrels and hinges in the arch that alternatively open and close up. When the structural deterioration becomes more severe, panels (d)–(f), structural damage starts accumulating despite the inversion of the ground motion, ultimately provoking the collapse for loss of equilibrium. Consistently with Remark 5, it is noticed that no dilatancy effect arises at the contacts between the blocks, even in presence of significant shear sliding.

In conclusion, the obtained numerical results show the computational merit of the proposed variational NSCD formulation in application to a full-scale structure subject to in-plane ground excitation. Differently than the previous benchmark problems, a complex dynamics characterized by a large number of impacts, also very close in time and yet not simultaneous, are naturally taken into account, providing accurate results of engineering interest.

4.5. Stone house

A fully three-dimensional problem concerning the dynamic behavior of a stone house is addressed in this section. The stone house is inspired by the masonry three-wall structure made up of rough stones of various sizes experimentally tested in [92]. The adopted geometrical model (Fig. 16) follows the simplified version proposed in [91], which approximately reproduces the average block size of the original mockup and assumes continuous horizontal joints. As a result, a more regular assembly of brick-shaped rigid blocks is obtained (a comparison with the numerical results from [91] is not pursued here, because the DEM commercial software 3DEC® therein used requires in input a conspicuous number of mechanical parameters that would be difficult to relate, without a dedicated calibration, to the only friction angle entering the present NSCD formulation). It is observed that the east wall of the stone house, corresponding to its façade, is characterized by a door opening and a timpanum. The two orthogonal walls have the same dimensions, with the north wall presenting a window opening. A Cartesian reference frame $(O; x, y, z)$ is introduced, such

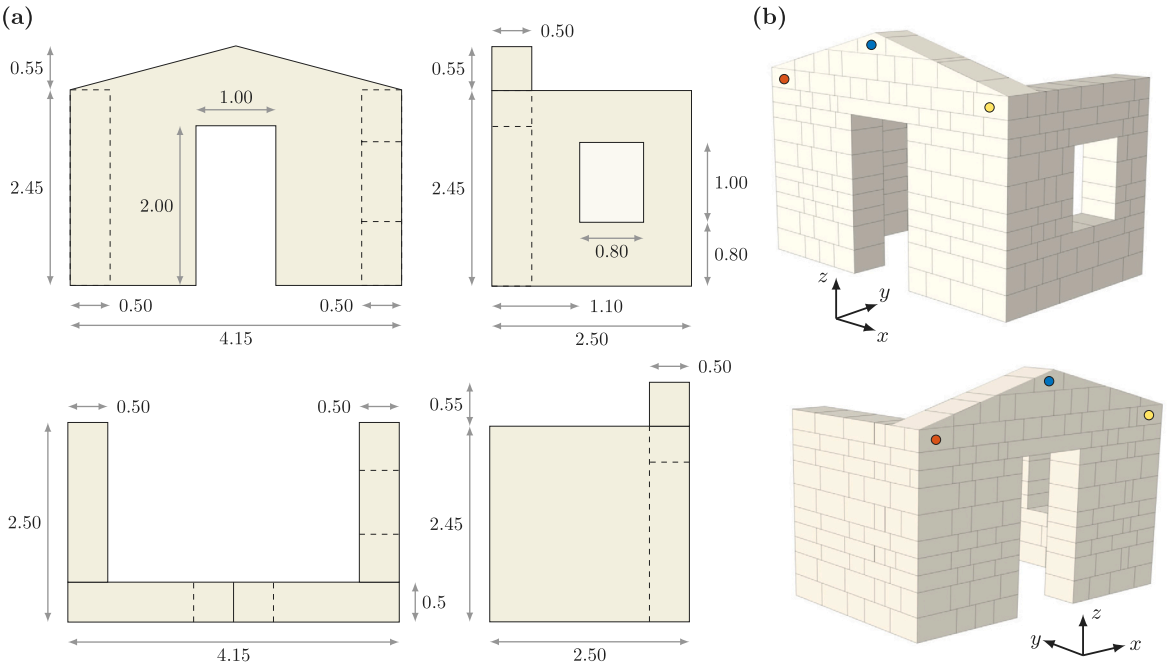

Fig. 16. Stone house: (a) geometric model of east, north, and south walls and of layout plan (clockwise-shown, with dimensions expressed in m), and (b) perspective views of the adopted numerical model [91,92]. (For interpretation of the references to color in this figure legend, the reader is referred to the web version of this article.)

that the x- and z-axes define the horizontal and vertical direction in the plane of the façade and the y-axis, pointing towards the orthogonal walls, defines the out-of-plane direction. The structure is constituted by $B = 191$ blocks, assumed to have uniform mass density. Three blocks of the façade are precisely monitored during the stone house motion, as pinpointed by markers in Fig. 16(b). They are referred to as the top central (blue marker), top south (red marker), and top north (yellow marker) blocks.

4.5.1. Time-history analysis

A time-history analysis of the stone house is initially performed. Specifically, the application of a one-sine impulse ground acceleration (Fig. 5(b)) of amplitude $a_{\mathrm{p}} = 0.8\,\mathrm{g}$ and half-period $t_{\mathrm{p}} = 0.20\,\mathrm{s}$ is considered along the negative y-direction. The corresponding pseudo-static seismic capacity, determined through a standard limit analysis procedure and implying the forward out-of-plane collapse of the façade, is $a_{\mathrm{p0}} = 0.372\,\mathrm{g}$. In Fig. 17(a), the time history of the (out-of-plane) y-displacement of the monitored blocks is reported, implying that the stone house façade oscillates due to the strong motion and eventually comes to rest in a slightly deformed configuration. Such a conclusion is consistent with the energy time history shown in Fig. 17(b). A phase lag is observed between the structural response and the ground motion, with potential-energy peaks approximately attained at time instants $t = \{0.25, 0.65\}$ s. The corresponding deformed configurations, alongside the one at the end of the simulation, are shown in Fig. 18. During the first excitation pulse, an in-plane backward rotation of a portion of the north wall, which is weakened by the window opening, is noticed. That also favors the formation of some cracks in the façade. Conversely, the second pulse activates a forward out-of-plane rotation motion of the façade, partially involving the orthogonal walls due to the interlocking between the blocks. Nonetheless, only minor residual damage is observed after the ground excitation.

The effect of a lower-frequency ground acceleration is then investigated by considering a one-sine impulse with half-period $t_{\mathrm{p}} = 0.40\,\mathrm{s}$ and unchanged acceleration amplitude $a_{\mathrm{p}} = 0.8\,\mathrm{g}$. The obtained results are shown in Figs. 19 and 20, adopting the same format introduced above. In this case, the first excitation pulse can already produce a severe in-plane backward rotation of the north wall. Afterward, the second pulse causes a forward out-of-plane rotational collapse of the façade, which practically evolves as a rigid body and drags down portions of the orthogonal walls.

As a general remark, it is observed that the dynamic behavior of the stone house is qualitatively governed by rotational-like mechanisms. That is a consequence of the adopted friction coefficient (corresponding to a friction angle of 35°), which is large enough to avoid significant sliding, and thus disaggregation, of the blocks. Moreover, for the quite complex three-dimensional masonry block structure under investigation, it is obtained that lower-frequency ground excitations are generally more dangerous than higher-frequency ones. That result is consistent with analogous conclusions drawn in the literature concerning simpler masonry block structures (e.g., see [33,34]).

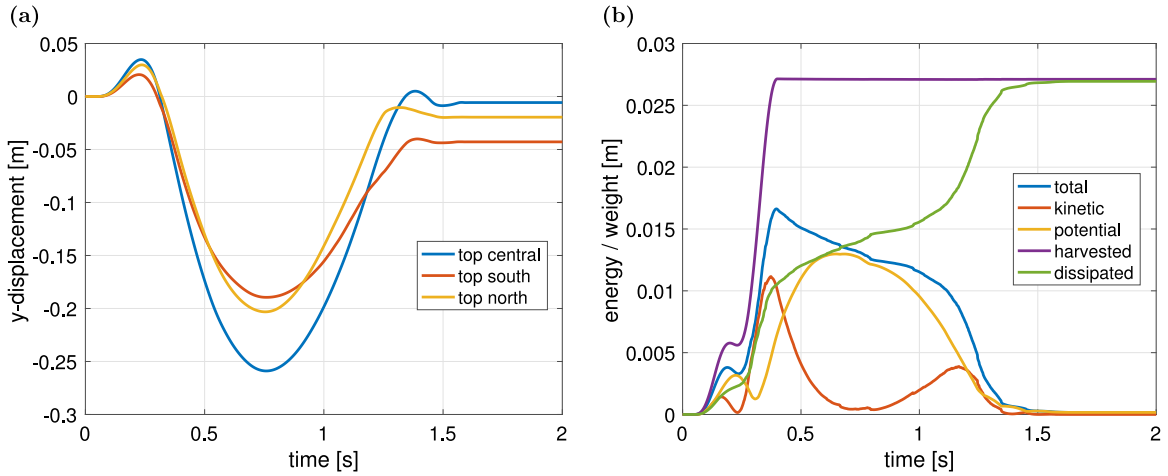

Fig. 17. Stone house: time history of (a) monitored block y-displacement and (b) energy per unit weight, in response to a one-sine impulse of amplitude $a_p = 0.8\,g$ and half-period $t_p = 0.20\,s$ along negative y-direction. (For interpretation of the references to color in this figure legend, the reader is referred to the web version of this article.)

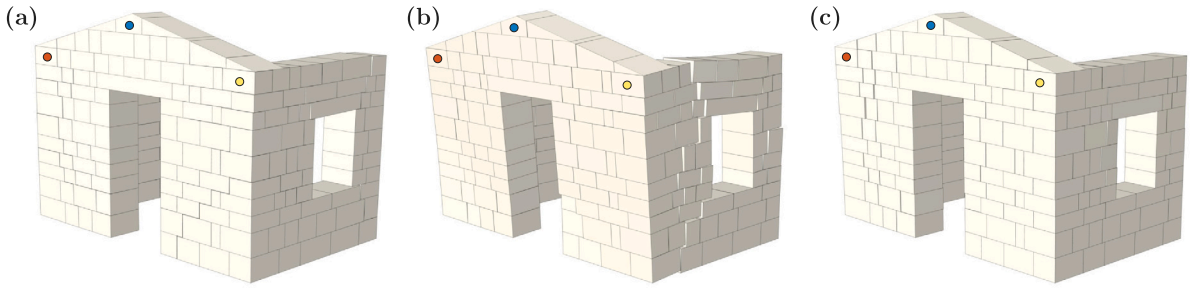

Fig. 18. Stone house: deformed configuration attained at potential-energy peaks at time instants (a)–(b) $t = \{0.25, 0.65\}$ s, and at final time instant (c) $t = 2\,s$, in response to a one-sine impulse of amplitude $a_p = 0.8\,g$ and half-period $t_p = 0.20\,s$ along negative y-direction. Blue, red, and yellow markers identify the monitored top central, top south, and top north blocks. (For interpretation of the references to color in this figure legend, the reader is referred to the web version of this article.)

4.5.2. Failure domain

The failure domains of the stone house in resisting a sinusoidal ground impulse excitation are investigated by systematically repeating the dynamic analysis in the previous section at varying the acceleration amplitude a_p and the half-period t_p of the applied impulse. For the typical ground excitation, the stone house motion is simulated for a duration $T = 2t_p + t^*$, exceeding the strong motion of the prescribed time $t^* = 2\,s$. Structural collapse is declared in case the potential energy of the structure measured from the foundation reduces by at least 20% with respect to the counterpart value in the initial configuration. Numerical evidence shows that such an adopted threshold also allows for consistently detecting partial structural collapses.

The results obtained adopting the friction coefficient $\mu = 0.7$ between the blocks are shown in Fig. 21(a), where dot markers are plotted for pairs (t_p, a_p) causing the stone house collapse. Different colors are adopted for markers relevant to a ground excitation in the positive (blue) or negative (red) y-direction. The boundaries of the resulting point clouds are interpreted as structural failure domains. For accelerations smaller than the pseudo-static seismic capacity (horizontal dashed lines), the stone house behaves as a rigid body integral to the ground. By contrast, a motion is initiated when larger accelerations are applied, with the structure recovering or collapsing for small or large half-period impulses, respectively. In particular, the boundary of the failure domains asymptotically approaches the pseudo-static seismic capacity for long impulse half-period.

It is observed that the failure domain for negative y-direction of the ground excitation is not monotonic with respect to the acceleration amplitude a_p for small half-periods t_p. Such a result, revealing the existence of small safe regions carving the unsafe one, is also observed for simpler masonry block structures (e.g., see [33,34]). Although that feature does not represent a numerical artifact, it is still recognized as a region of complex response from the structure. Since the direction of the ground excitation is not known in advance and in order to guarantee the monotonicity with respect to the acceleration amplitude, for safety, it is proposed to consider as the structural failure domain the convex hull of the union of the point clouds relevant to both the ground excitation directions.

The descending failure domain is reported in Fig. 21(b), where a comparison at varying the friction coefficient between the blocks for the selected values $\mu = \{0.3, 0.5, 0.7\}$ is also delivered. Since the pseudo-static seismic capacity increases with the friction

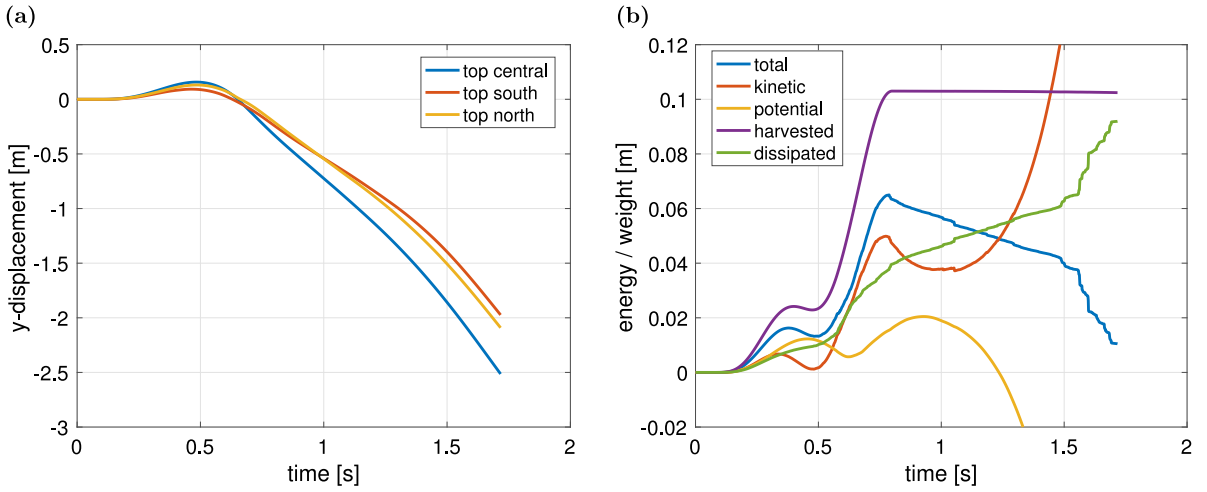

Fig. 19. Stone house: time history of (a) monitored block y-displacement and (b) energy per unit weight, in response to a one-sine impulse of amplitude $a_p = 0.8\,g$ and half-period $t_p = 0.40\,s$ along negative y-direction. (For interpretation of the references to color in this figure legend, the reader is referred to the web version of this article.)

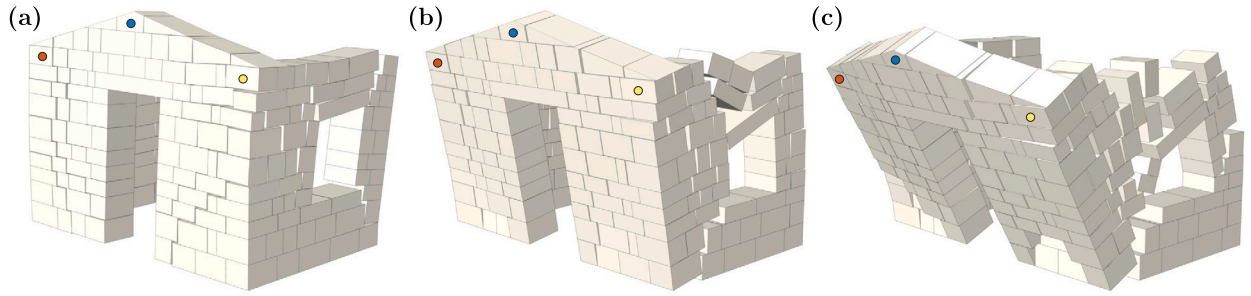

Fig. 20. Stone house: deformed configuration attained at time instants (a)–(c) $t = \{0.5, 0.9, 1.3\}$ s, in response to a one-sine impulse of amplitude $a_p = 0.8\,g$ and half-period $t_p = 0.40\,s$ along negative y-direction. Blue, red, and yellow markers identify the monitored top central, top south, and top north blocks. (For interpretation of the references to color in this figure legend, the reader is referred to the web version of this article.)

coefficient (as indicated by the horizontal dashed lines), the dynamic resistance of the stone house appears to correspondingly improve for long impulse half-period (the failure domains slightly shift upwards for increasing μ). By contrast, when high-frequency excitations are concerned, it is observed that a smaller friction coefficient reduces the structural vulnerability (the failure domains shift rightwards for decreasing μ). Within the present context, where a purely frictional behavior is assumed at the block interfaces, that result follows from a structural isolation effect due to significant sliding occurring at the interface between the blocks of the first and second bottom masonry courses when the friction coefficient is sufficiently small.

Overall, it is confirmed that the failure domains of the stone house under sinusoidal ground impulse excitation are in line with that shown by simpler masonry structures, as found in the literature (e.g., see [33,34]).

4.5.3. Fragility function

The stone house case study is finally exploited to assess the applicability of the proposed variational NSCD formulation in predicting the dynamic behavior of historical masonry structures under earthquake excitation. Specifically, the estimation of a fragility function for the stone house is targeted here, as required in several seismic assessment procedures (e.g., see [93,94]). A fragility function characterizes the probability $\mathbb{P}(C|\mathrm{IM} \leq x)$ that a ground motion with intensity measure $\mathrm{IM} \leq x$ produces the collapse C of the structure. By adopting the form of a lognormal cumulative distribution function, the fragility function is thus defined as (e.g., see [95]):

$$\mathbb{P}(C|\mathrm{IM} \leq x) = \boldsymbol{\Phi}\left(\frac{\ln(x/\theta)}{\beta}\right), \tag{24}$$

in which $\boldsymbol{\Phi}$ is the standard normal cumulative distribution function, whereas θ and β respectively denote the median of IM values associated with the onset of collapse and the standard deviation of $\ln \mathrm{IM}$.

The suite of ground motions given in FEMA P695 is considered in the present investigation [96]. It consists of 56 near-field and 44 far-field records that are applied to the structure along the y-direction. The peak ground acceleration PGA is chosen as the

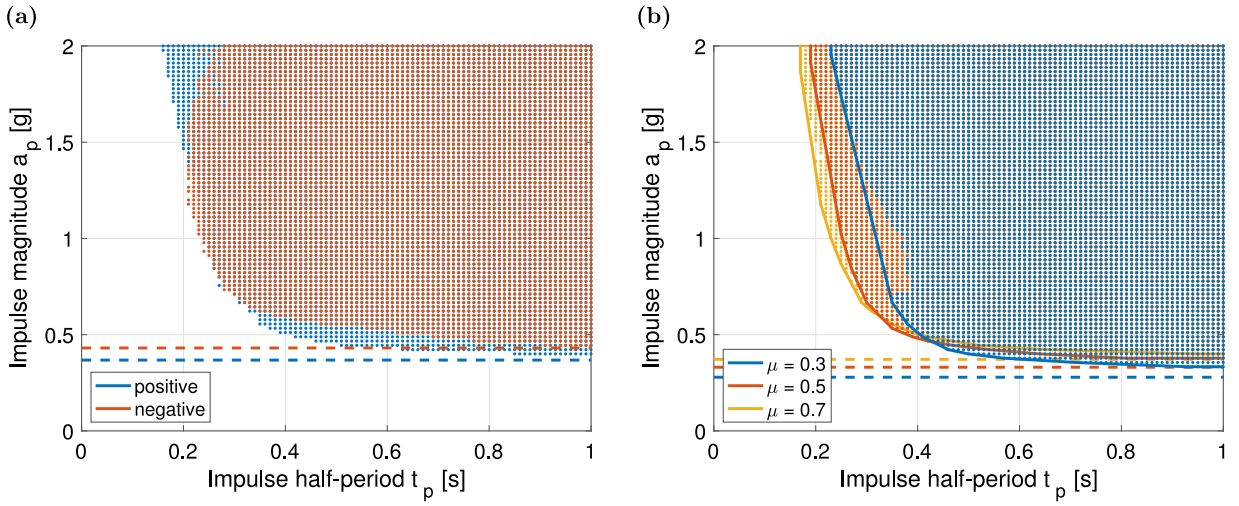

Fig. 21. Stone house: (a) failure domain for a one-sine impulse of amplitude a_p and half-period t_p along positive or negative y-direction assuming friction coefficient $\mu = 0.7$ at the interface between the blocks and (b) failure domain obtained as union of the counterpart domains for positive or negative y-direction at varying the friction coefficient μ at the interface between the blocks. (For interpretation of the references to color in this figure legend, the reader is referred to the web version of this article.)

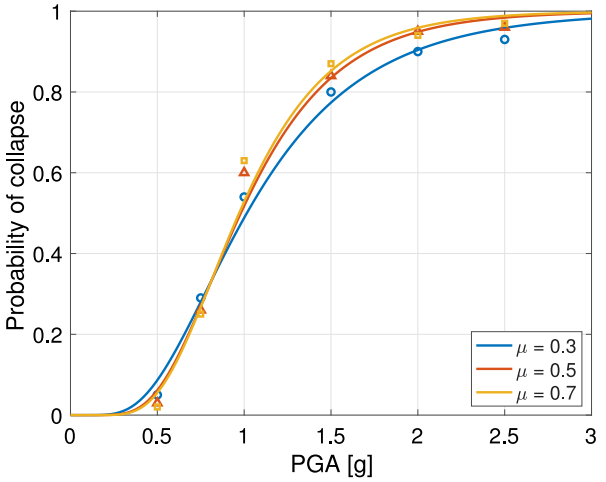

Fig. 22. Stone house: observed fractions of collapse as a function of the PGA (markers) and estimated log-normal fragility functions (solid lines), for the FEMA P6955 suite of 56 near-field and 44 far-field records [96] along the y-direction. Selected values of the friction coefficient μ at the interface between the blocks are considered. (For interpretation of the references to color in this figure legend, the reader is referred to the web version of this article.)

intensity measure IM of the ground motions (several different choices can be considered, e.g., see [98,99]). In order to estimate the fragility function parameters θ and β, a multiple stripe analysis is resorted to (e.g., see [95]). Within that approach, scaled versions of each ground motion are considered to match a discrete set of intensity measure IM values, and a dynamic analysis is performed for each scaled ground motion to determine whether structural collapse occurs. In numerical simulations, the time step $\Delta t = 0.0025$ s has been adopted, corresponding to the minimum sampling rate of the records, and the structural collapse has been identified based on the potential energy criterion introduced in the previous section. The obtained numerical results are shown in Fig. 22, where markers identify the fraction of collapses predicted for the investigated values $\{0.5, 0.75, 1, 1.5, 2, 2.5\}$ of the PGA (in units of g) for the values $\mu = \{0.3, 0.5, 0.7\}$ of the friction coefficient between the blocks.

The estimates of the fragility function parameters θ and β are then obtained by maximizing the log-likelihood function (e.g., see [95]):

$$\mathcal{L} = \sum_j \left\{ \ln\binom{n_j}{z_j} + z_j \ln \Phi\left(\frac{\ln\left(x_j/\theta\right)}{\beta}\right) + \left(n_j - z_j\right) \ln\left[1 - \Phi\left(\frac{\ln\left(x_j/\theta\right)}{\beta}\right)\right] \right\}, \tag{25}$$

where x_j denotes the typical intensity measure IM value in the investigated discrete set, and z_j denotes the number of collapses in the corresponding n_j ground motions. Such a log-likelihood function is obtained by assuming that the collapse under a ground motion is

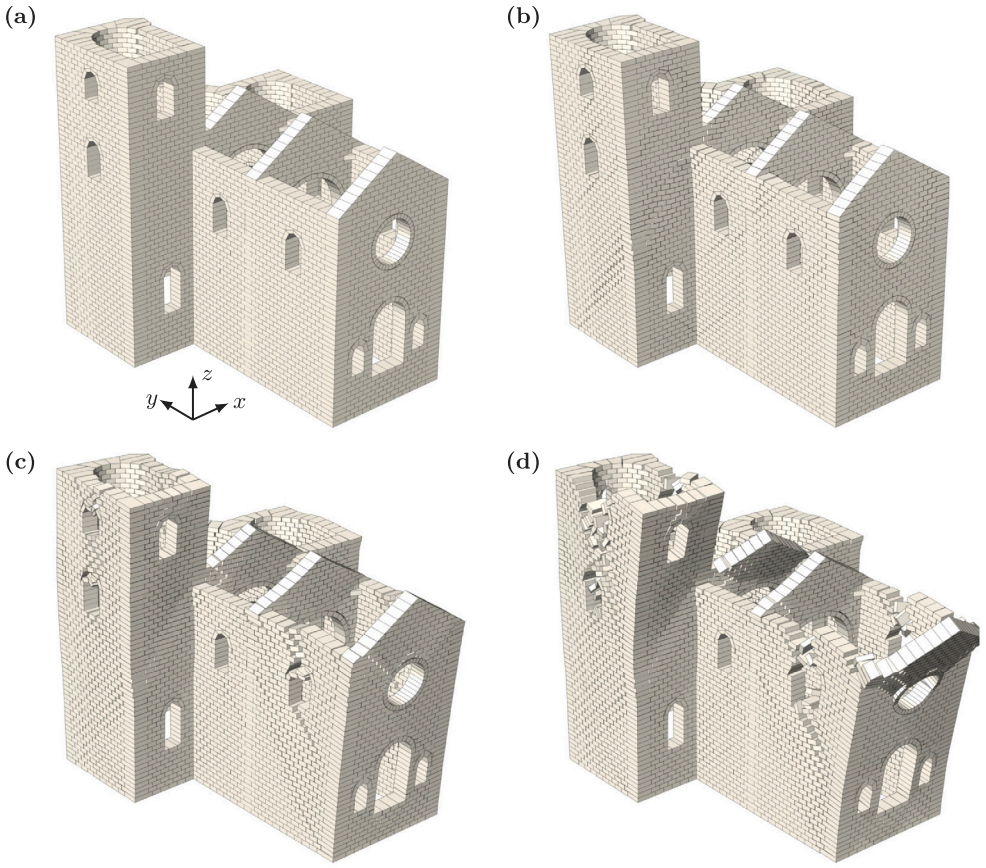

Fig. 23. Historical church: (a) perspective view of the adopted numerical model [97] and deformed configurations attained at time instants (b)–(d) $t = \{0.6, 1.2, 2\}$ s, in response to a one-sine impulse of amplitude $a_{\mathrm{p}} = 1\,\mathrm{g}$ and half-period $t_{\mathrm{p}} = 0.40\,\mathrm{s}$ along negative y-direction.

independent of the collapse under other ground motions, i.e., that the number z_j of collapses out of n_j ground motions with IM $= x_j$ is given by a binomial distribution, and using the lognormal cumulative distribution function model (24) for the fragility function. In practice, a generalized linear regression of the data (x_j, z_j, n_j) with a probit link function is performed, which is equivalent to solving problem (25) (e.g., see [100]). The obtained estimates of the fragility function parameters are $\theta = \{1.015, 0.981, 0.971\}$ and $\beta = \{0.520, 0.436, 0.416\}$ respectively for the values $\mu = \{0.3, 0.5, 0.7\}$ of the friction coefficient at the interfaces between the blocks. The corresponding fragility functions are shown in Fig. 22. It is noticed that while the fragility functions for $\mu = 0.5$ and $\mu = 0.7$ are similar, an improved seismic resistance is achieved for large PGA values in the case of $\mu = 0.3$. That result may be motived by the same seismic isolation effect observed under one-sine impulse excitation.

In conclusion, the present numerical results demonstrate the merit of the proposed variational NSCD computational approach in addressing the dynamic response of historical masonry structures under earthquake excitation, thus enabling seismic applications with practical engineering interest.

4.6. Historical church

In order to challenge the proposed NSCD formulation on a masonry structure comprising thousands of blocks, the dynamic response of the historical church shown in Fig. 23(a) is addressed. The adopted numerical model closely follows the one investigated under static loading conditions in [97]. In detail, the church layout is in the form of a Latin Cross, characterized by a single nave about 18 m long and a transept 14 m large, with a chapel and a bell tower located at the apse sides. The church and the bell tower are 14 m and 17 m high, respectively. The structure is constituted by $B = 5161$ blocks of uniform mass density. A Cartesian reference frame $(O; x, y, z)$ is considered, such that the x- and y-axes respectively define the transverse and longitudinal directions of the church, and the z-axis corresponds to the vertical direction.

A time-history analysis of the church is performed under a one-sine impulse of amplitude $a_{\mathrm{p}} = 1\,\mathrm{g}$ and half-period $t_{\mathrm{p}} = 0.40\,\mathrm{s}$ along the negative y-direction. In passing, it is noticed that the longitudinal pseudo-static seismic capacity of the church, determined by standard limit analysis and producing the out-of-plane collapse of the façade, is $a_{\mathrm{p0}} = 0.238\,\mathrm{g}$ (in agreement with the value 0.237 g

found in [97]). Fig. 23(b) shows the deformed configuration attained by the church at the time instant $t = 0.6$ s. That is representative of the effect of the first excitation pulse, which mainly induces a backward rotation of the bell tower, as highlighted by the formation of diagonal cracks in its lateral wall, and some damage to the church façace. Subsequently, as illustrated by the deformed configuration at time instants $t = \{1.2, 2\}$ s reported in Figs. 23(c)–(d), the second excitation pulse implies the forward collapse of the upper part of the bell tower and the church façace, with severe damage of the church lateral walls.

Finally, the obtained numerical results prove the potentialities of the proposed variational NSCD computational approach to predict the dynamic behavior of complex historical masonry constructions involving thousands of blocks and evolving through an intricate sequence of block contacts and collisions.

5. Conclusions

A variational formulation of the non-smooth contact dynamics approach has been presented, aimed at numerically predicting the dynamic response of historical masonry structures made up of 3D rigid blocks and undergoing ground excitation. In line with the non-smooth contact dynamics method, the equations of motion have been set in a time-discrete impulse-theorem format, resorting to block velocities and contact impulses as the problem unknowns. A unilateral-frictional contact law with an associative flow rule has been assumed between the blocks and enforced as conic constraints on the relative velocities of antagonist contact points. As the advantage of adopting an associative flow rule, the equivalence of the time-discrete dynamic problem with a saddle-point variational formulation has been shown, from which purely kinematic and static functionals have been obtained. The proposed numerical method requires, at each time step, performing a collision detection that identifies antagonist contact points based on the given structural configuration, solving a second-order conic programming problem to compute block velocities and contact impulses, and updating the structural configuration for the solution to advance in time. An optimization software available in the literature, implementing a primal-dual interior-point method, has been resorted to for the solution of the time-step optimization problem, leveraging the convex setting of the formulation to handle also large-scale problems robustly and efficiently. Numerical results have been presented to test the computational performances of the proposed approach. Specifically, numerical evidence that the present method implies no dilatancy at the contacts between the blocks and is consistent with event-driven solutions based on the classical Housner impact model has been provided in three benchmark problems. Moreover, the dynamic response, failure domains, and fragility functions of real-size masonry structures subjected to ground impulse or earthquake excitation have been explored. The obtained results prove the accuracy, robustness, and efficiency of the method to serve as a reliable computational tool for the dynamic analysis and seismic assessment of historical masonry constructions of engineering interest.

CRediT authorship contribution statement

Nicola A. Nodargi: Writing – review & editing, Writing – original draft, Visualization, Validation, Software, Methodology, Investigation, Funding acquisition, Formal analysis, Conceptualization. **Paolo Bisegna:** Writing – review & editing, Validation, Software, Methodology, Conceptualization.

Declaration of competing interest

The authors declare that they have no known competing financial interests or personal relationships that could have appeared to influence the work reported in this paper.

Data availability

Data will be made available on request.

Acknowledgments

The financial support of European Union – Next Generation EU, Italian Ministry of University and Research, PRIN 2022 program, Italy, project "COMˆ3D-CREATE" (grant number: 2022SMSZZ9_002) is gratefully acknowledged.

Appendix. Linearized rotational equilibrium equation

This section is devoted to the linearization of the time-discrete rotational equations of motion $(3)_2$. In particular, the nonlinear map $\boldsymbol{\omega}^b \mapsto \mathbf{J}^b\,\boldsymbol{\omega}^b$ relevant to the typical block b is considered. Its Jacobian $\overline{\mathbf{H}}^b$ is given by:

$$\overline{\mathbf{H}}^b\,\Delta\boldsymbol{\omega}^b = \mathbf{J}^b\Delta\boldsymbol{\omega}^b + \left(\Delta\mathbf{R}^b\mathbf{R}^{bT}\right)\mathbf{J}^b\boldsymbol{\omega}^b + \mathbf{J}^b\left(\Delta\mathbf{R}^b\mathbf{R}^{bT}\right)^T\boldsymbol{\omega}^b, \tag{A.1}$$

involving the linearized rotation matrix in the term $\Delta\mathbf{R}^b\mathbf{R}^{bT}$. That satisfies (e.g., see [101]):

$$\Delta\mathbf{R}^b\mathbf{R}^{bT} = \mathrm{skw}\left(\mathbf{B}^b\,\Delta\boldsymbol{\omega}^b\right), \quad \mathbf{B}^b = \boldsymbol{I} + \frac{1-\cos\omega^b}{\left(\omega^b\right)^2}\,\boldsymbol{\Omega}^b + \frac{\omega^b-\sin\omega^b}{\left(\omega^b\right)^3}\,\left(\boldsymbol{\Omega}^b\right)^2, \tag{A.2}$$

where the position $\omega^b = \|\boldsymbol{\omega}^b\|$ has been introduced. The positive semidefinite part $\mathbf{H}^b$ of the Jacobian $\overline{\mathbf{H}}^b$ is obtained as:

$$\overline{\mathbf{H}}^b_{\text{sym}} = \frac{1}{2}\left(\overline{\mathbf{H}}^b + \overline{\mathbf{H}}^{bT}\right) = \boldsymbol{V}^b \boldsymbol{D}^b \boldsymbol{V}^{bT}, \quad \mathbf{H}^b = \boldsymbol{V}^b \boldsymbol{D}^b_+ \boldsymbol{V}^{bT}, \tag{A.3}$$

i.e., by replacing the diagonal matrix $\boldsymbol{D}^b$ involved in the eigendecomposition of its symmetric part $\overline{\mathbf{H}}^b_{\text{sym}}$ with the positive part $\boldsymbol{D}^b_+$. Finally, the matrix $\mathbf{H}$ is given by:

$$\mathbf{H} = \text{diag}\left(\mathbf{H}^1; \dots; \mathbf{H}^B\right), \tag{A.4}$$

to be used in the linearized rotational equilibrium equations (8).

References

[1] J. Heyman, The stone skeleton, Int. J. Solids Struct. 2 (2) (1966) 249–279, http://dx.doi.org/10.1016/0020-7683(66)90018-7.

[2] R.K. Livesley, Limit analysis of structures formed from rigid blocks, Internat. J. Numer. Methods Engrg. 12 (12) (1978) 1853–1871, http://dx.doi.org/10.1002/nme.1620121207.

[3] M. Como, Statics of historic masonry constructions, third ed., Springer Series in Solid and Structural Mechanics, vol. 9, Springer International, Cham, 2017, http://dx.doi.org/10.1007/978-3-319-54738-1.

[4] G.W. Housner, The behavior of inverted pendulum structures during earthquakes, Bull. Seismol. Soc. Am. 53 (2) (1963) 403–417, http://dx.doi.org/10.1785/BSSA0530020403.

[5] M.J.N. Priestley, R.J. Evison, A.J. Carr, Seismic response of structures free to rock on their foundations, Bull. New Zealand Soc. Earthq. Eng. 11 (3) (1978) 141–150.

[6] C.S. Yim, A.K. Chopra, J. Penzien, Rocking response of rigid blocks to earthquakes, Earthq. Eng. Struct. Dyn. 8 (6) (1980) 565–587, http://dx.doi.org/10.1002/eqe.4290080606.

[7] Y. Ishiyama, Motions of rigid bodies and criteria for overturning by earthquake excitations, Earthq. Eng. Struct. Dyn. 10 (5) (1982) 635–650, http://dx.doi.org/10.1002/eqe.4290100502.

[8] S.J. Hogan, On the dynamics of rigid-block motion under harmonic forcing, Proc. R. Soc. A 425 (1989) 441–476, http://dx.doi.org/10.1098/rspa.1989.0114.

[9] A. Sinopoli, Dynamic analysis of a stone column excited by a sine wave ground motion, Appl. Mech. Rev. 44 (11) (1991) S246–S255, http://dx.doi.org/10.1115/1.3121361.

[10] P.R. Lipscombe, S. Pellegrino, Free rocking of prismatic blocks, J. Eng. Mech. 119 (7) (1993) 1387–1410, http://dx.doi.org/10.1061/(ASCE)0733-9399(1993)119:7(1387).

[11] B. Shi, A. Anooshehpoor, Y. Zeng, J.N. Brune, Rocking and overturning of precariously balanced rocks by earthquakes, Bull. Seismol. Soc. Am. 86 (5) (1996) 1364–1371.

[12] J. Zhang, N. Makris, Rocking response of free-standing blocks under cycloidal pulses, J. Eng. Mech. 127 (5) (2001) 473–483, http://dx.doi.org/10.1061/(ASCE)0733-9399(2001)127:5(473).

[13] N. Makris, D. Konstantinidis, The rocking spectrum and the limitations of practical design methodologies, Earthq. Eng. Struct. Dyn. 32 (2) (2003) 265–289, http://dx.doi.org/10.1002/eqe.223.

[14] F. Peña, F. Prieto, P.B. Lourenço, A. Campos Costa, J. Lemos, On the dynamics of rocking motion of single rigid-block structures, Earthq. Eng. Struct. Dyn. 36 (15) (2007) 2383–2399, http://dx.doi.org/10.1002/eqe.739.

[15] M.A. Elgawady, Q. Ma, J.W. Butterworth, J. Ingham, Effects of interface material on the performance of free rocking blocks, Earthq. Eng. Struct. Dyn. 40 (4) (2011) 375–392, http://dx.doi.org/10.1002/eqe.1025.

[16] H. Zhang, B. Brogliato, C. Liu, Dynamics of planar rocking-blocks with Coulomb friction and unilateral constraints: comparisons between experimental and numerical data, Multibody Syst. Dyn. 32 (2014) 1–25, http://dx.doi.org/10.1007/s11044-013-9356-9.

[17] E. Voyagaki, I.N. Psycharis, G. Mylonakis, Complex response of a rocking block to a full-cycle pulse, J. Eng. Mech. 140 (6) (2014) http://dx.doi.org/10.1061/(ASCE)EM.1943-7889.0000712.

[18] A.N. Kounadis, On the rocking-sliding instability of rigid blocks under ground excitation: Some new findings, Soil Dyn. Earthq. Eng. 75 (2015) 246–258, http://dx.doi.org/10.1016/j.soildyn.2015.03.026.

[19] T. Ther, L.P. Kollár, Overturning of rigid blocks for earthquake excitation, Bull. Earthq. Eng. 16 (3) (2018) 1607–1631, http://dx.doi.org/10.1007/s10518-017-0238-z.

[20] S. Coccia, M. Como, F. Di Carlo, The slender rigid block: Archetype for the seismic analysis of masonry structures, J. Earthq. Eng. (2022) 1–25, http://dx.doi.org/10.1080/13632469.2022.2121337.

[21] A.M. D'Altri, G. Vlachakis, S. de Miranda, P.B. Lourenço, Rocking block simulation based on numerical dissipation, Nonlinear Dynam. (2024) http://dx.doi.org/10.1007/s11071-024-09974-1.

[22] I.J. Oppenheim, The masonry arch as a four-link mechanism under base motion, Earthq. Eng. Struct. Dyn. 21 (11) (1992) 1005–1017, http://dx.doi.org/10.1002/eqe.4290211105.

[23] L. De Lorenzis, M. DeJong, J. Ochsendorf, Failure of masonry arches under impulse base motion, Earthq. Eng. Struct. Dyn. 36 (14) (2007) 2119–2136, http://dx.doi.org/10.1002/eqe.719.

[24] N. Makris, M.F. Vassiliou, Planar rocking response and stability analysis of an array of free-standing columns capped with a freely supported rigid beam, Earthq. Eng. Struct. Dyn. 42 (3) (2012) 431–449, http://dx.doi.org/10.1002/eqe.2222.

[25] M.J. DeJong, E.G. Dimitrakopoulos, Dynamically equivalent rocking structures, Earthq. Eng. Struct. Dyn. 43 (10) (2014) 1543–1563, http://dx.doi.org/10.1002/eqe.2410.

[26] G. Misseri, L. Rovero, Parametric investigation on the dynamic behaviour of masonry pointed arches, Arch. Appl. Mech. 87 (3) (2017) 385–404, http://dx.doi.org/10.1007/s00419-016-1199-4.

[27] L. Severini, N. Cavalagli, M. DeJong, V. Gusella, Dynamic response of masonry arch with geometrical irregularities subjected to a pulse-type ground motion, Nonlinear Dynam. 91 (2018) 609–624, http://dx.doi.org/10.1007/s11071-017-3897-z.

[28] M.F. Funari, A. Mehrotra, P.B. Lourenço, A tool for the rapid seismic assessment of historic masonry structures based on limit analysis optimisation and rocking dynamics, Appl. Sci. 11 (2021) 942, http://dx.doi.org/10.3390/app11030942.

[29] P. Bisegna, S. Coccia, M. Como, N.A. Nodargi, A novel impact model for the rocking motion of masonry arches, Meccanica 58 (2023) 2079–2093, http://dx.doi.org/10.1007/s11012-023-01714-w.

[30] R. Allen, I. Oppenheim, A. Parker, J. Bielak, On the dynamic response of rigid body assemblies, Earthq. Eng. Struct. Dyn. 14 (6) (1986) 861–876, http://dx.doi.org/10.1002/eqe.4290140604.

[31] I.N. Psycharis, Dynamic behaviour of rocking two-block assemblies, Earthq. Eng. Struct. Dyn. 19 (4) (1990) 555–575, http://dx.doi.org/10.1002/eqe.4290190407.

[32] P.D. Spanos, P.C. Roussis, N.P.A. Politis, Dynamic analysis of stacked rigid blocks, Soil Dyn. Earthq. Eng. 21 (7) (2001) 559–578, http://dx.doi.org/10.1016/S0267-7261(01)00038-0.

[33] T. Ther, L.P. Kollár, Model for multiblock columns subjected to base excitation, Earthq. Eng. Struct. Dyn. 47 (2) (2018) 418–437, http://dx.doi.org/10.1002/eqe.2957.

[34] L.P. Kollár, T. Ther, Numerical model and dynamic analysis of multi degree of freedom masonry arches, Earthq. Eng. Struct. Dyn. 48 (7) (2019) 709–730, http://dx.doi.org/10.1002/eqe.3158.

[35] N.A. Nodargi, P. Bisegna, A variational event-driven approach for the dynamic analysis of multi-block historical masonry structures under ground excitation, Eng. Struct. 306 (2024) 117804, http://dx.doi.org/10.1016/j.engstruct.2024.117804.

[36] D. Zulli, A. Contento, A. Di Egidio, 3D model of rigid block with a rectangular base subject to pulse-type excitation, Int. J. Non-Linear Mech. 47 (2012) 679–687, http://dx.doi.org/10.1016/j.ijnonlinmec.2011.11.004.

[37] M.N. Chatzis, A.W. Smyth, Modeling of the 3D rocking problem, Int. J. Non-Linear Mech. 47 (2012) 85–98, http://dx.doi.org/10.1016/j.ijnonlinmec.2012.02.004.

[38] M.F. Vassiliou, S. Burger, M. Egger, J.A. Bachmann, M. Broccardo, B. Stojadinović, The three-dimensional behavior of inverted pendulum cylindrical structures during earthquakes, Earthq. Eng. Struct. Dyn. 46 (14) (2017) 2261–2280, http://dx.doi.org/10.1002/eqe.2903.

[39] Y. Bao, Y. Xu, B. Wu, Modeling and validation of three-dimensional sliding-rocking rigid block subjected to earthquake excitation, Earthq. Eng. Struct. Dyn. 51 (2022) 2858–2879, http://dx.doi.org/10.1002/eqe.3705.

[40] C. Pradhan, A. Banerjee, R. Roy, Evolution of a 3D model for free-standing rigid blocks and its behavior under base excitations, Int. J. Non-Linear Mech. 142 (2022) 103992, http://dx.doi.org/10.1016/j.ijnonlinmec.2022.103992.

[41] P. Várkonyi, M. Kocsis, T. Ther, Rigid impacts of three-dimensional rocking structures, Nonlinear Dynam. 107 (2022) 1839–1858, http://dx.doi.org/10.1007/s11071-021-06934-x.

[42] J.J. Moreau, Unilateral contact and dry friction in finite freedom dynamics, in: J.J. Moreau, P.D. Panagiotopoulos (Eds.), Nonsmooth Mechanics and Applications, in: International Centre for Mechanical Sciences, vol. 302, Springer, Vienna, 1988, pp. 1–82, http://dx.doi.org/10.1007/978-3-7091-2624-0_1.

[43] V. Acary, B. Brogliato, Numerical methods for nonsmooth dynamical systems, Lecture Notes in Applied and Computational Mechanics, vol. 35, Springer-Verlag, Berlin Heidelberg, 2008.

[44] P. Flores, Contact mechanics for dynamical systems: a comprehensive review, Multibody Syst. Dyn. 54 (2021) 127–177, http://dx.doi.org/10.1007/s11044-021-09803-y.

[45] B. Brogliato, Nonsmooth mechanics, third ed., Communications and Control Engineering, Springer, Cham, 2016, http://dx.doi.org/10.1007/978-3-319-28664-8.

[46] J.J. Moreau, Numerical aspectsof the sweeping proces, Comput. Methods Appl. Mech. Engrg. 177 (3–4) (1999) 329–349, http://dx.doi.org/10.1016/S0045-7825(98)00387-9.

[47] M. Jean, The non-smooth contact dynamics method, Comput. Methods Appl. Mech. Engrg. 177 (1999) 235–257, http://dx.doi.org/10.1016/S0045-7825(98)00383-1.

[48] D.E. Stewart, J.C. Trinkle, An implicit time-stepping scheme for rigid body dynamics with inelastic collisions and Coulomb friction, Internat. J. Numer. Methods Engrg. 39 (1996) 2673–2691, http://dx.doi.org/10.1002/(SICI)1097-0207(19960815)39:15<2673::AID-NME972>3.0.CO;2-I.

[49] R.W. Cottle, J.S. Pang, R.E. Stone, The linear complementarity problem, Classics in Applied Mathematics, vol. 60, SIAM, 2009.

[50] Y. Nesterov, Introductory lectures on convex optimization, first ed., Applied Optimization, Springer, New York, 2003.

[51] D.E. Stewart, Convergence of a time-stepping scheme for rigid-body dynamics and resolution of Ppainlevé's problem, Arch. Ration. Mech. Anal. 145 (1998) 215–260, http://dx.doi.org/10.1007/s002050050129.

[52] V. Acary, Projected event-capturing time-stepping schemes for nonsmooth mechanical systems with unilateral contact and Coulomb's friction, Comput. Methods Appl. Mech. Engrg. 256 (2013) 224–250, http://dx.doi.org/10.1016/j.cma.2012.12.012.

[53] O. Brüls, V. Acary, A. Cardona, Simultaneous enforcement of constraints at position and velocity levels in the nonsmooth generalized-α scheme, Comput. Methods Appl. Mech. Engrg. 281 (2014) 131–161, http://dx.doi.org/10.1016/j.cma.2014.07.025.

[54] T. Schindler, S. Rezaei, J. Kursawe, V. Acary, Half-explicit timestepping schemes on velocity level based on time-discontinuous Galerkin methods, Comput. Methods Appl. Mech. Engrg. 290 (2015) 250–276, http://dx.doi.org/10.1016/j.cma.2015.03.001.

[55] J. Luo, X. Xu, X. Liu, Z. Wu, A nonsmooth modified symplectic integration scheme for frictional contact dynamics of rigid-flexible multibody systems, Comput. Methods Appl. Mech. Engrg. 420 (2024) 116726, http://dx.doi.org/10.1016/j.cma.2023.116726.

[56] G. Capobianco, J. Harsch, S. Leyendecker, Lobatto-type variational integrators for mechanical systems with frictional contact, Comput. Methods Appl. Mech. Engrg. 418 (2024) 116496, http://dx.doi.org/10.1016/j.cma.2023.116496.

[57] A. Charles, F. Casenave, C. Glocker, A catching-up algorithm for multibody dynamics with impacts and dry friction, Comput. Methods Appl. Mech. Engrg. 334 (2018) 208–237, http://dx.doi.org/10.1016/j.cma.2018.01.054.

[58] S. Abide, M. Barboteu, S. Cherkaoui, S. Dumont, A semi-smooth Newton and primal-dual active set method for non-smooth contact dynamics, Comput. Methods Appl. Mech. Engrg. 387 (2021) 114153, http://dx.doi.org/10.1016/j.cma.2021.114153.

[59] M. Barboteu, F. Bonaldi, S. Dumont, C. Mahmoud, An energy-consistent discretization of hyper-viscoelastic contact models for soft tissues, Comput. Methods Appl. Mech. Engrg. 421 (2024) 116785, http://dx.doi.org/10.1016/j.cma.2024.116785.

[60] F. Dubois, M. Jean, The non smooth contact dynamic method: recent LMGC90 software developments and application, in: P. Wriggers, U. Nackenhorst (Eds.), Analysis and Simulation of Contact Problems, in: Lecture Notes in Applied and Computational Mechanics, vol. 27, Springer, Berlin, Heidelberg, 2006, pp. 375–378, http://dx.doi.org/10.1007/3-540-31761-9_44.

[61] B. Chetouane, F. Dubois, M. Vinches, C. Bohatier, NSCD discrete element method for modelling masonry structures, Internat. J. Numer. Methods Engrg. 64 (2005) 65–94, http://dx.doi.org/10.1002/nme.1358.

[62] G. Lancioni, D. Gentilucci, E. Quagliarini, S. Lenci, Seismic vulnerability of ancient stone arches by using a numerical model based on the non-smooth contact dynamics method, Eng. Struct. 119 (2016) 110–121, http://dx.doi.org/10.1016/j.engstruct.2016.04.001.

[63] F. Clementi, A. Ferrante, E. Giordano, F. Dubois, S. Lenci, Damage assessment of ancient masonry churches stroked by the central Italy earthquakes of 2016 by the non-smooth contact dynamics method, Bull. Earthq. Eng. 18 (2020) 455–486, http://dx.doi.org/10.1007/s10518-019-00613-4.

[64] A. Ferrante, D. Loverdos, F. Clementi, G. Milani, A. Formisano, S. Lenci, V. Sarhosis, Discontinuous approaches for nonlinear dynamic analyses of an ancient masonry tower, Eng. Struct. 230 (2021) 111626, http://dx.doi.org/10.1016/j.engstruct.2020.111626.

[65] M. Anitescu, Optimization-based simulation of nonsmooth rigid multibody dynamics, Math. Program. 105 (2006) 113–143, http://dx.doi.org/10.1007/s10107-005-0590-7.

[66] K. Krabbenhoft, A.V. Lyamin, J. Huang, V.M. da Silva, Granular contact dynamics using mathematical programming methods, Comput. Geotech. 43 (2012) 165–176, http://dx.doi.org/10.1016/j.compgeo.2012.02.006.

[67] F.P.A. Portioli, L. Cascini, Contact dynamics of masonry block structures using mathematical programming, J. Earthq. Eng. 22 (2018) 94–115, http://dx.doi.org/10.1080/13632469.2016.1217801 94.

[68] F.P.A. Portioli, Rigid block modelling of historic masonry structures using mathematical programming: a unified formulation for non-linear time history, static pushover and limit equilibrium analysis, Bull. Earthq. Eng. 18 (2020) 211–239, http://dx.doi.org/10.1007/s10518-019-00722-0.
[69] F.P.A. Portioli, M. Godio, C. Calderini, P.B. Lourenço, A variational rigid-block modeling approach to nonlinear elastic and kinematic analysis of failure mechanisms in historic masonry structures subjected to lateral loads, Earthq. Eng. Struct. Dyn. 50 (2021) 3332–3354, http://dx.doi.org/10.1002/eqe.3512.
[70] F.P.A. Portioli, L. Cascini, R. Landolfo, P.B. Lourenço, An optimization-based rigid block modeling approach to seismic assessment of dry-joint masonry structures subjected to settlements, Soil Dyn. Earthq. Eng. 166 (2023) 107760, http://dx.doi.org/10.1016/j.soildyn.2023.107760.
[71] F.P.A. Portioli, DynABlock_2D: An optimization-based MATLAB application for rocking dynamics, nonlinear static and limit analysis of masonry block structures, SoftwareX 23 (2023) 101454, http://dx.doi.org/10.1016/j.softx.2023.101454.
[72] V. Beatini, G. Royer-Carfagni, A. Tasora, A regularized non-smooth contact dynamics approach for architectural masonry structures, Comput. Struct. 187 (2017) 88–100, http://dx.doi.org/10.1016/j.compstruc.2017.02.002.
[73] V. Beatini, G. Royer-Carfagni, A. Tasora, Modeling the shear failure of segmental arches, Int. J. Solids Struct. 158 (2019) 21–39, http://dx.doi.org/10.1016/j.ijsolstr.2018.08.023.
[74] V. Beatini, G. Royer-Carfagni, A. Tasora, A non-smooth-contact-dynamics analysis of Brunelleschi's cupola: an octagonal vault or a circular dome? Meccanica 54 (2019) 525–547, http://dx.doi.org/10.1007/s11012-018-00934-9.
[75] P.A. Cundall, O.D.L. Strack, A discrete numerical model for granular assemblies, Geotechnique 29 (1) (1979) 47–65, http://dx.doi.org/10.1680/geot.1979.29.1.47.
[76] F. Dubois, V. Acary, M. Jean, The contact dynamics method: A nonsmooth story, C. R. Mec. 346 (2018) 247–262, http://dx.doi.org/10.1016/j.crme.2017.12.009.
[77] I.N. Psycharis, D.Y. Papastamatiou, A.P. Alexandris, Parametric investigation of the stability of classical columns under harmonic and earthquake excitations, Earthq. Eng. Struct. Dyn. 29 (8) (2000) 1093–1109, http://dx.doi.org/10.1002/1096-9845(200008)29:8<1093::AID-EQE953>3.0.CO;2-S.
[78] P. Komodromos, L. Papaloizou, P. Polycarpou, Simulation of the response of ancient columns under harmonic and earthquake excitations, Eng. Struct. 30 (8) (2008) 2154–2164, http://dx.doi.org/10.1016/j.engstruct.2007.11.004.
[79] R. Dimitri, L. De Lorenzis, G. Zavarise, Numerical study on the dynamic behavior of masonry columns and arches on buttresses with the discrete element method, Eng. Struct. 33 (12) (2011) 3172–3188, http://dx.doi.org/10.1016/j.engstruct.2011.08.018.
[80] I.N. Psycharis, Seismic reliability assessment of classical columns subjected to near-fault ground motions, Earthq. Eng. Struct. Dyn. 42 (2013) 2061–2079, http://dx.doi.org/10.1002/eqe.2312.
[81] F. Gobbin, G. de Felice, J.V. Lemos, Numerical procedures for the analysis of collapse mechanisms of masonry structures using discrete element modelling, Eng. Struct. 246 (2021) 113047, http://dx.doi.org/10.1016/j.engstruct.2021.113047.
[82] J.V. Lemos, K. Bagi, Discrete element modeling, in: K. Bagi, M. Angelillo (Eds.), Discrete Computational Mechanics of Masonry Structures, in: CISM International Centre for Mechanical Sciences, vol. 609, Springer, Cham, 2023, pp. 189–232, http://dx.doi.org/10.1007/978-3-031-32476-5_5.
[83] MOSEK ApS, The MOSEK optimization toolbox for MATLAB. Release 10.1.12, 2023, URL https://docs.mosek.com/latest/toolbox.pdf.
[84] F. Alizadeh, D. Goldfarb, Second-order cone programming, Math. Program. Ser B 95 (2003) 3–51, http://dx.doi.org/10.1007/s10107-002-0339-5.
[85] E. Andersen, C. Roos, T. Terlaky, On implementing a primal-dual interior-point method for conic quadratic optimization, Math. Program. Ser B 95 (2003) 249–277, http://dx.doi.org/10.1007/s10107-002-0349-3.
[86] E.G. Gilbert, D.W. Johnson, S.S. Keerthi, A fast procedure for computing the distance between complex objects in three-dimensional space, IEEE J. Robot. Autom. 4 (2) (1988) 193–203, http://dx.doi.org/10.1109/56.2083.
[87] M. Montanari, N. Petrinic, E. Barbieri, Improving the GJK algorithm for faster and more reliable distance queries between convex objects, ACM Trans. Graph. 36 (3) (2017) 30.
[88] Itasca Consulting Group, Inc., 3DEC documentation, 2024, URL https://docs.itascacg.com/3dec700/contents.html.
[89] A. Orosz, K. Bagi, Comparison of contact treatment methods for rigid polyhedral discrete element models, Int. J. Rock Mech. Min. Sci. 170 (2023) 105550, http://dx.doi.org/10.1016/j.ijrmms.2023.105550.
[90] T. Ther, L.P. Kollár, Refinement of Housner's model on rocking blocks, Bull. Earthq. Eng. 15 (5) (2017) 2305–2319, http://dx.doi.org/10.1007/s10518-016-0048-8.
[91] J.V. Lemos, A. Campos-Costa, Simulation of shake table tests on out-of-plane masonry buildings. part (V): Discrete element approach, Int. J. Archit. Herit. 11 (1) (2017) 117–124, http://dx.doi.org/10.1080/15583058.2016.1237587.
[92] P.X. Candeias, A. Campos-Costa, N. Mendes, A.A. Costa, P.B. Lourenço, Experimental assessment of the out-of-plane performance of masonry buildings through shaking table tests, Int. J. Archit. Herit. 11 (1) (2017) 31–58, http://dx.doi.org/10.1080/15583058.2016.1238975.
[93] A. Kita, N. Cavalagli, M.G. Masciotta, P.B. Lourenço, F. Ubertini, Rapid post-earthquake damage localization and quantification in masonry structures through multidimensional non-linear seismic IDA, Eng. Struct. 219 (2020) 110841, http://dx.doi.org/10.1016/j.engstruct.2020.110841.
[94] M. Nale, F. Minghini, A. Chiozzi, A. Tralli, Fragility functions for local failure mechanisms in unreinforced masonry buildings: a typological study in Ferrara, Italy, Bull. Earthq. Eng. 19 (2021) 6049–6079, http://dx.doi.org/10.1007/s10518-021-01199-6.
[95] J.W. Baker, Efficient analytical fragility function fitting using dynamic structural analysis, Earthq. Spectra 31 (1) (2015) 579–599, http://dx.doi.org/10.1193/021113EQS025M.
[96] FEMA, Quantification of Building Seismic Performance Factors: Component Equivalency Methodology, Tech. Rep., Federal Emergency Management Agency, Washington, DC, 2009.
[97] M. Malena, F. Portioli, R. Gagliardo, G. Tomaselli, L. Cascini, G. de Felice, Collapse mechanism analysis of historic masonry structures subjected to lateral loads: A comparison between continuous and discrete models, Comput. Struct. 220 (2019) 14–31, http://dx.doi.org/10.1016/j.compstruc.2019.04.005.
[98] A.I. Giouvanidis, E.G. Dimitrakopoulos, Rocking amplification and strong-motion duration, Earthq. Eng. Struct. Dyn. 47 (10) (2018) 2094–2116, http://dx.doi.org/10.1002/eqe.3058.
[99] M. Sieber, M.F. Vassiliou, I. Anastasopoulos, Intensity measures, fragility analysis and dimensionality reduction of rocking under far-field ground motions, Earthq. Eng. Struct. Dyn. 51 (15) (2022) 3639–3657, http://dx.doi.org/10.1002/eqe.3740.
[100] A. Agresti, An introduction to categorical data analysis, third ed., Wiley Series in Probability and Statistics, Wiley, Hoboken, NJ, 2019.
[101] A. Eriksson, C. Pacoste, Element formulation and numerical techniques for stability problems in shells, Comput. Methods Appl. Mech. Engrg. 191 (35) (2002) 3775–3810, http://dx.doi.org/10.1016/S0045-7825(02)00288-8.